DOI:10.15774/PPKE.ITK.2018.003

SPIN-WAVE-BASED COMPUTING

A Dissertation

Submitted to the
Roska Tamás Doctoral School of Sciences and Technology
in Partial Fulfillment of the Requirements
for the Degree of

Doctor of Philosophy

by
Ádám Papp

Supervisor:
Árpád Csurgay

Supervisors at the University of Notre Dame:
Wolfgang Porod
György Csaba

Pázmány Péter Catholic University
Faculty of Information Technology and Bionics
Budapest, 2017

DOI:10.15774/PPKE.ITK.2018.003

Abstract

Today's computing devices are mostly based on CMOS technology, built on Boolean logic, and almost exclusively represent signals electrically. The steady exponential growth of CMOS made it dominant in the past few decades, however the scale down now approaches hard limits and it encounters more and more difficulties to keep up with Moore's law. Though many believe that transistor technologies will be able to overcome these issues – as they did so far – it is worth to consider other technologies, even ones that were earlier outcompeted by CMOS.

We investigated the usage of spin waves for computing purposes. Our approach is to directly use spin waves for wave-computing algorithms as opposed to designing novel logic gates using spin-wave signals – which has been the more typical approach recently. We borrowed ideas from the already well established optical computing theory, but instead of using optical waves, we redesigned these concepts for spin waves. We proposed spin-wave phase shifters and lenses, and investigated different types of sources for spin-wave generation. Based on these components a spin-wave Fourier transformation and filtering device were designed, and we believe that these designs can be further expanded to holographic pattern matching devices, or other special-purpose signal-processing hardware accelerators. We verified our proof-of-principle designs using micromagnetic simulations and we are currently working on experimental demonstrations of the feasibility of our concepts.

An alternative approach is described in Appendix B, where instead of spin waves, domain walls carry the signal in our Threshold Gate design based on out-of-plane polarized nanomagnetic dots with nucleation sides specified by irradiation. In addition this can be used to realize logic gates more compactly – as we demonstrated for a Full Adder design – and it has the potential to be used in non-Boolean computing, e.g. neural networks.

DOI:10.15774/PPKE.ITK.2018.003

Kivonat

Napjaink számítógépei túlnyomóan a CMOS technológián alapulnak, Boolean logikára épülnek, és szinte kizárólag elektromos jeleket használnak. A CMOS technológia gyors és töretlen növekedésével az elmúlt évtizedekben egyeduralkodóvá nőtte ki magát, de a tranzisztorok méretének további csökkentése egyre inkább megközelíti a fizikai korlátokat. Ennek következtében a Moore törvény szerinti növekedéssel már egyre nehezebb lépést tartani. Ugyan sokan dolgoznak azon, hogy a tranzisztor technológia túl tudjon lendülni ezeken a gátakon – ahogy eddig is sikerült fenntartani a fejlődés ütemét –, érdemes egészen más alapú technológiákat is megvizsgálni, akár olyanokat is, amelyeket korábban már kiszorított a CMOS technológia.

Ebben a disszertációban a spinhullámok alkalmazási lehetőségeit vizsgáltuk számító- és jelfeldolgozó eszközökben. A spinhullámokat elsősorban hullámszámítógép-algoritmusok megvalósítása szempontjából vizsgáljuk, szemben az általánosabb megközelítéssel, melyben a spinhullámokat új típusú logikai kapcsoló megvalósíthatósága szempontjából vizsgálják. Az alapvető elveket az optikai számítógép architektúrák régmúltú és jelentős irodalmából kölcsönöztük, de fény, illetve elektromágneses hullámok helyett spinhullámokat alkalmazunk. Javaslatot teszünk spinhullám fázistoló rácsok és lencsék megvalósítására, és megvizsgáltunk különböző típusú spinhullám keltő technológiákat. Ezekre az elemekre alapozva spinhullámokkal működő Fourier transzformációt és jelszűrést végző eszközöket terveztünk. Ezekhez hasonló módon egyéb speciális célú jelfeldolgozó eszközök, hardveres gyorsítók valósíthatók meg, például holografikus mintázatfelismerő eszköz. A működési elvet demonstráló eszközterveket mikromágneses szimulációkkal igazoltuk, továbbá dolgozunk a kísérleti demonstráción is.

Egy a fentiektől eltérő megközelítésre adunk példát a B függelékben, ahol spinhullámok helyett doménfalak továbbítják a jelet a Threshold Gate alapú eszközben. A doménfalak vékony mágneses vezetékekben terjednek, melyekben a mágnesezettség iránya a síkra merőleges, és a doménfalak keltésének helye ion besugárzással meghatározott. Threshold Gate alapon kompaktabb nanomágneses logikák hozhatók létre, melyet egy Full Adder-en keresztül szemléltetünk, továbbá nem Boolean típusú logikák is építhetők belőle, például neurális hálózatok.

DOI:10.15774/PPKE.ITK.2018.003

Contents

DOI:10.15774/PPKE.ITK.2018.003

DOI:10.15774/PPKE.ITK.2018.003

List of Figures

DOI:10.15774/PPKE.ITK.2018.003

DOI:10.15774/PPKE.ITK.2018.003

DOI:10.15774/PPKE.ITK.2018.003

DOI:10.15774/PPKE.ITK.2018.003

List of Tables

DOI:10.15774/PPKE.ITK.2018.003

ACKNOWLEDGMENTS

I would like to thank my advisors, Dr. György Csaba, Dr. Wolfgang Porod, and Dr. Árpád Csurgay (Pázmány Péter Catholic University, Budapest, Hungary) for their direction, and for helpful discussions. I am also thankful to my fellow graduate students, Himadri Dey and Hadrian Aquino for the provided samples for measurements and for fruitful discussions.

This research was supported by the NSF/SRC grant 'Nanoelectrics Beyond 2020'.

DOI:10.15774/PPKE.ITK.2018.003

Chapter 1

INTRODUCTION

Magnetic computing has found special interest in the last decade and has been intensely researched as a candidate for beyond-CMOS technologies. Today's computing is mostly based on electrical signals and charges, and spin is almost always only used as an information storage element. However, it has been demonstrated that magnetization state [2], [3] as well as spin-wave amplitude and phase [4], [5], [6], [7], [8] may be used for information transfer and processing.

Spin-based devices offer relatively low power consumption, medium to high speed, intrinsic non-volatility, and small footprint, while typically they do not require exotic materials or new fabrication technologies. Spin waves are propagating excitations of the magnetic media, typically in ferromagnetic or ferrimagnetic materials. Spin waves are different from electromagnetic waves in a number of ways. They are non-linear (can be used in linear region with small amplitudes), require a magnetic medium to propagate, they have relatively short wavelength (potentially $\lambda < 100$ nm) in the frequency region of 1-100 GHz. These properties make spin waves attractive for on-chip applications. Most research recently has been conducted towards creating a new logical switch, which could replace today's CMOS based gates. However, spin waves may be used for analog information processing, wave computing, either used in the linear region or exploiting the nonlinearity of spin waves. Good summaries of the current directions in the field are [9] and [10].

We believe that an especially attractive application area for spin waves could be signal processing applications. There is a wide class of problems that require extensive use of linear transformations (such as spectral analysis), and these require extensive computational power. These problems are usually highly parallelizable and there are multiple dedicated device classes used as co-processors to accelerate these calculations, such as digital signal processors (DSP) or graphics processing units (GPU). These hardwares are usually based on CMOS technology and have a specialized limited instruction set that is optimized for certain problems. Typical applications include image processing, data mining, spectral decomposition, etc. These applications usually require high-speed processing of enormous amounts of data with a single instruction. A very good fit for this problem types could be the use of wave-computing computational models instead of Boolean-logic-based arithmetics. These exploit the highly parallel nature of wave propagation and are able to process data by linear interference of waves. Information can be encoded in either the phase or the amplitude of waves, which can be in time domain or spatial. By designing appropriate interference patterns of the waves, it is possible to implement complex linear transformations. The underlying physical representation of the waves can be any linear or approximately linear interaction, e.g. spin waves or electromagnetic waves. Optical computing is an important example, in this case

DOI:10.15774/PPKE.ITK.2018.003

the interference of light is used for computation, and there are proposed emulated wave-computing devices as well based on digital architectures[11]. Our choice of representation is the use of spin waves, and we will show that such wave-computing algorithms are indeed feasible using spin waves and argue about the benefits of using spin waves, keeping in mind their limitations as well. Wave interference can be used for computation in other ways as well, an interesting example that uses electron diffraction to create a novel field effect transistor is [12].

The idea of using magnetic materials and spin waves for microwave applications is not new, and summary of such concepts was already provided in [13]. However with today's nanofabrication capabilities a new horizon opens with much smaller scale devices and new application areas. With the increasing number of communication devices, the dawn of the internet of things (IoT[14]), the need for low power filters for wireless communication purposes increases. The need for higher bandwidth pushes the technology towards higher frequencies, but silicon technology has its frequency limits and there are no low-power transistor based circuits at several GHz frequencies. Spin waves can be used up to a hundred GHz and possibly in the soft-THz regime, with submicron wavelengths which enables compact integration.

Conversion between electric and magnetic signals is a very important part of magnetic device design, since the conversion technologies represent the connection between electronic circuitry and spin-based circuitry. The power that drives magnetic devices also usually comes from electric sources, since there are no good methods for storing and conducting power directly in magnetic field. There is a number of promising technologies already established or under research for magnetic-electric conversion, e.g. Spin Torque Oscillators, Spin Hall Effect, Giant Magneto Resistance, Magnetic Tunneling Junctions, MagnetoElectric cells. Unfortunately, so far none of this technologies achieved a breakthrough in conversion efficiency, thus, the input and output power dissipation is still on of the main problems of magnetic designs.

In this dissertation, we will start with a quick introduction to the physics of magnetism and spin-waves on a level that is absolutely necessary to understand the device operations. In Chapter 3, we explore the basic building blocks of spin-wave devices which are important for the realization of wave-computing algorithms. We show that most simple devices known in optics may be realized by spin waves as well. In Chapter 4, we present algorithms that may be realized by spin waves and we verify the operation of these devices by micromagnetic simulations. Chapter 5 is a case study for a special application area, namely microwave spectral decomposition, where we show a compact design which we believe that effectively demonstrates the simplicity and power of spin-wave-based designs. In Chapter 6, we explore the limitations of the magnetic manipulation of spin waves in insulating magnetic films, and propose a possible solution to inject spin waves into insulators via metallic magnetic layers. The interaction of an insulator-metal layer is investigated using micromagnetic simulations. Part of the Candidate's research was a construction of an FMR measurement setup, which is an indispensable tool for magnetic sample characterizations. The considerations and steps of the design and results of preliminary test measurements are included in Chapter 7. Ap-

DOI:10.15774/PPKE.ITK.2018.003

pendix A contains the design considerations and results of our preliminary spin-wave measurements (the measurements were done in collaboration). Appendix B describes a threshold logic gate design based on nanomagnetic logic. Although it is not strictly connected to the rest of the dissertation as it is not a spin-wave device, it is part of the Candidate's early PhD research, and it is an example of the use of magnetic domain walls for computation.

This Dissertation is mainly based on papers already published by the Candidate, and it shares a large amount of the content of these papers.

DOI:10.15774/PPKE.ITK.2018.003

Chapter 2

INTRODUCTION TO MICROMAGNETISM

The goal of this chapter is to provide a short introduction to the theory of micromagnetism and spin waves. Micromagnetic theory describes the micro-nano scale behavior of the magnetic materials, but it can not be applied on the atomic or molecular level, where quantum effects need to be considered as well.

2.1 Effective field concept

The magnetic properties of materials arise mainly from the spin of the elementary particles in the atom (most significantly the electron and nuclear spin) and the orbital angular momentum of the electrons. It is usually convenient to denote the spatial distribution of the magnetic moments using a vector field $\mathbf{M}(\mathbf{r}, t)$.

A magnetic field applied on a magnetic moment creates a torque on it. This magnetic field can be an external field, e.g. created by a current, or the magnetic field of the elementary magnetic moments in the material. The latter is called demagnetizing field since the demagnetizing energy is minimal if the magnetic moments point in opposite directions, thus the net magnetic field of the sample diminishes.

Another important phenomenon is the exchange interaction, which is a purely quantum mechanical effect acting on the elementary particle level. In ferromagnets, the exchange energy is lowest if the electron spins are parallel to each other, and highest if they are antiparallel. The exchange interaction causes the spins to arrange in the same direction in the material, giving rise to magnetic domains. Although the exchange interaction is a quantum effect, it is convenient to represent it as a classical magnetic field in the micromagnetic model.

There are multiple types of magnetic anisotropies, i.e. directional preferences of the magnetization, which may be caused by the crystal structure (magnetocrystalline anisotropy), tension on the lattice (magnetoelastic anisotropy), or between different types of materials (exchange anisotropy).

The effective magnetic field $\mathbf{H}_{eff}(\mathbf{r}, t) = \mathbf{H}_{ext} + \mathbf{H}_{demag} + \mathbf{H}_{exch} + \mathbf{H}_{aniso}$ is the sum of the fields above, which together act on the magnetic distribution $\mathbf{M}(\mathbf{r}, t)$.

2.2 Micromagnetic dynamics

A magnetic field creates a torque on a magnetic moment, which causes it to precess about the magnetic field direction at the Larmor frequency. This precession occurs as long as the field acts, however in real world there is always some damping which causes the magnetic

DOI:10.15774/PPKE.ITK.2018.003

momentum to eventually spiral in to the direction of the magnetic field as can be seen in Figure 2.1. This process is described by the Landau-Lifshitz-Gilbert equation:

$$\frac{d\mathbf{M}}{dt} = -|\gamma|\,\mathbf{M}\times\mathbf{H}_{eff} + \frac{\alpha}{M_S}\left(\mathbf{M}\times\frac{d\mathbf{M}}{dt}\right) \tag{2.1}$$

where γ is the Gilbert gyromagnetic ratio, α is the damping constant and $M_S = |\mathbf{M}(\mathbf{r},t)|$ is the saturation magnetization. The first term on the right side is the precessional term, the second is the damping term.

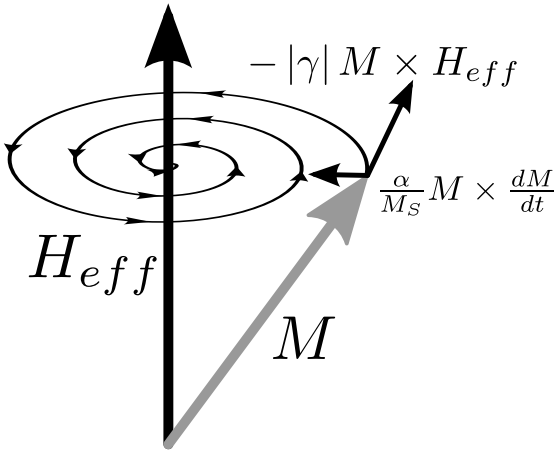

Figure 2.1. Precession of the magnetic moment around the effective field.

2.3 Micromagnetic simulations

Solving the Landau-Lifshitz-Gilbert equation analytically is only feasible for simple cases, and for complex designs one has to use a numerical approach. We used OOMMF[15] for most of the simulations, which is a well established and widely known micromagnetic solver. For larger designs, GPU accelerated calculators can be used, and we also used MuMax3 [16] in some cases.

When solving numerically, the design has to be divided into cells which are assumed to be single domain. Typical cell sizes we used are 5 nm in every dimension, which is sufficiently small if we consider that the single domain limit is on the order of 100 nm. Spin waves at very high frequencies can have wavelength as small as a few nanometers, which would require much higher resolution, and thus enormous computing capacity. Also, the micromagnetic model is not valid in the sub-nanometer regime. Typically we simulate spin waves with wavelengths on the order of a hundred nanometer, this range of wavelengths is

DOI:10.15774/PPKE.ITK.2018.003

probably the lower limit of what can be generated and detected efficiently using currently available technologies.

2.4 Ferromagnetic resonance

If we apply a transverse microwave-frequency magnetic field to a magnetic moment on its resonance frequency it can absorb energy from the field. In practice, one has to saturate the magnetic sample so that there are no domains (i.e. all magnetic moment point the same direction). This way all the magnetic moments in the sample will resonate at the same frequency, thus absorbing a measurable amount of energy from the microwave field. This enables us to calculate the saturation magnetization based on the measured resonance frequency, and we can also estimate the damping coefficient in the film from the resonance peak linewidth.

In ferromagnetic materials, the shape of the sample plays an important role in the effective field. The demagnetizing field in the sample is different for different shapes, and one generally needs numerical calculations to take into account the field contribution from every part of the geometry. For simple geometries like an ellipsoid it is simple to calculate demagnetization factors N_x, N_y, N_z, and the components of the demagnetizing field can be written as $H_x = -N_x M_x, H_y = -N_y M_y, H_z = -N_z M_z$.

If we assume that the sample is saturated in the z-direction by an external field H_0 and thus $\frac{dM_z}{dt} \approx 0$, and we neglect the effect of damping, the components of the spin equation of motion become

$$\frac{dM_x}{dt} = \gamma \left(H_0 + \left(N_y - N_z\right) M_s\right) M_y \tag{2.2}$$

$$\frac{dM_y}{dt} = -\gamma \left(H_0 + \left(N_x - N_z\right) M_s\right) M_x \tag{2.3}$$

Assuming solutions with time dependence $e^{-i\omega t}$, we solve for the ferromagnetic resonance (FMR) frequency:

$$\omega_0^2 = \gamma^2 \left(H_0 + \left(N_y - N_z\right) M_s\right) \left(H_0 + \left(N_x - N_z\right) M_s\right). \tag{2.4}$$

Let us now examine a few specific geometries, for which the demagnetizing factors are easy to calculate. For a sphere $N_x = N_y = N_z$, so $\omega_0 = \gamma H_0$, i.e. the resonance frequency does not depend on the saturation magnetization and there is no cutoff frequency. We can approximate a film in the xy plane with a flat ellipsoid, and with perpendicular H_0 (pointing in z direction) we get $N_x = N_y = 0, N_z = 1$ and so the frequency:

$$\omega_0 = \gamma \left(H_0 - M_s\right) \tag{2.5}$$

If the film lies in the xz plane with H_0 pointing in z direction (in-plane field), $N_x = N_z = 0, N_y = 1$ so:

$$\omega_0 = \gamma \sqrt{H_0 \left(H_0 + M_s\right)}. \tag{2.6}$$

The FMR frequency derived above corresponds to the uniform mode. If the magnetic sample is thick enough spin waves that are created on the surfaces can resonate if the film

DOI:10.15774/PPKE.ITK.2018.003

thickness is an integer multiple of the half-wavelength, this is called Spin Wave Resonance. From these examples, it can be seen, that there are two main factors that define the spin-wave resonance frequency, one of them is the saturation magnetization which is a material parameter, the other is the external field, which is practically limited to a few teslas.

2.5 Spin waves

Through the coupling between the individual spins, excitations can travel in a magnetic material in the form of spin waves. There are basically two coupling mechanisms that play a role in the formation of spin waves: the demagnetizing field and the exchange interaction. It is customary to talk about two types of spin waves, dipole dominated and exchange dominated spin waves, based on the dominant coupling interaction. There are actually always both types of coupling present, but for short wavelengths exchange interaction dominates, while dipole interaction dominates for long distances.

For computing and signal processing purposes the exchange dominated waves are more suitable as these have shorter wavelength which allows larger scale integration. In this work we will concentrate on spin waves in thin magnetic films, as these are more compatible with planar fabrication technologies.

Unlike optical waves, spin waves do not have a linear dispersion relation, and they do not allow wave propagation below a cutoff frequency. This cutoff frequency is typically a few gigahertz, thus spin-wave devices would operate in the several gigahertz range, up to approximately one terahertz, although such high frequencies would require very high magnetic fields.

There are also major differences between spin waves and electromagnetic waves. The spin-wave dispersion relation is nonlinear and its characteristics strongly depend on material parameters and externally applied magnetic fields and may be 'engineered' by the appropriate choice of these parameters. Spin-wave wavelengths as small as a few-ten nanometers may correspond to microwave (5-100 GHz) frequencies, while microwave electromagnetic waves have much larger wavelengths, in the millimeter-centimeter range. Electromagnetic waves are isotropic in most media, while spin-wave propagation can be isotropic or strongly anisotropic depending on the relative orientation of **M** magnetization and the **k** wavevector. Electromagnetic waves travel with no damping in vacuum, and with very small damping in many dielectrics. Spin waves can not propagate in vacuum and are strongly damped in most ferromagnetic metals but may propagate reasonably large distances (thousand times wavelength) in ferrites (such as yttrium iron garnet, YIG) [17].

Let us examine a good approximation for the dispersion relation of spin waves in a saturated bulk magnet [18]:

$$\omega = \sqrt{\omega_H \left(\omega_H + \omega_M \sin^2\theta\right)} \tag{2.7}$$

where $\omega_H = \gamma\mu_0 H_0 + \omega_M \lambda_{ex} k^2$, $\omega_M = \gamma\mu_0 M_S$, $\lambda_{ex} = \frac{2A_{exch}}{\mu_0 M_S^2}$, γ is the gyromagnetic ratio, μ_0 is the vacuum permeability, M_S is the saturation magnetization, H_0 is the total internal field, A_{exch} is the exchange coefficient, k is the wavenumber and θ is the angle between the prop-

DOI:10.15774/PPKE.ITK.2018.003

agation direction and the static component of the magnetization vector. Here we assumed that the magnet is saturated, i.e. the static component of the magnetization vector is pointed along the direction of the effective magnetic field.

The first observation we can make is that this dispersion relation is not linear, but rather close to parabolic, in the limit of $\theta = 0$ it simplifies to a parabola. Secondly, there is an $\omega_0 = \gamma\mu_0 H_0$ cutoff frequency, and below this frequency there is no spin-wave propagation. Also, the dispersion relation described by Eq. 2.7 depends on the angle (θ) between the direction of wave propagation and the magnetization. This dependence results in an anisotropic wave propagation for in-plane magnetized films, but not in out-of-plane films, since in that case the out-of-plane (normal) vector is perpendicular to every wavevector in plane.

If we consider a thin magnetic film with thickness comparable to the spin-wave wavelength, the reflections from the boundaries of the film will result in different propagating modes. A general dispersion relation for thin films with thickness d can be written in a similar form [19]:

$$\omega = \sqrt{\omega_H \left(\omega_H + \omega_M F\left(\phi, \psi\right)\right)} \tag{2.8}$$

where

$$F\left(\phi, \psi\right) = P + \sin^2\psi \left[1 - P\left(1 + \cos^2\phi\right) + \omega_M \frac{P\left(1-P\right)\sin^2\phi}{\omega_H}\right] \tag{2.9}$$

and

$$P = 1 - \frac{1 - e^{-kd}}{kd}. \tag{2.10}$$

Here ψ represents the angle between the magnetization direction and the film normal, and ϕ denotes the angle between the wave vector and the projection of the magnetization vector to the film plane.

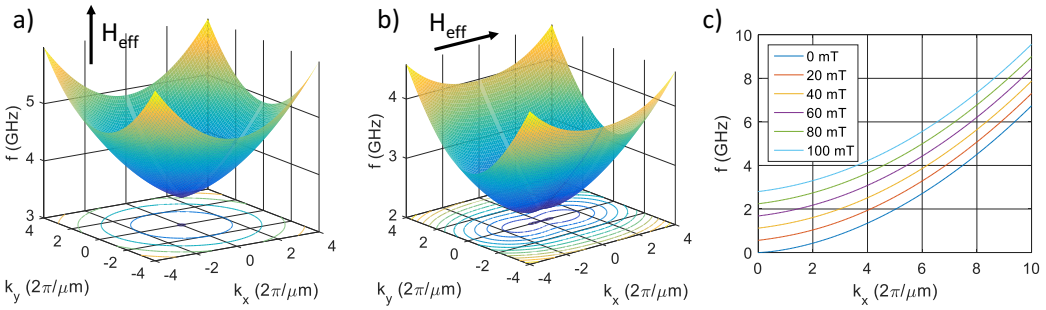

Figure 2.2. Dispersion in a $d = 20$ nm thick YIG film with a) an external field $H_{ext} = 300$ mT applied perpendicular to the film b) an external field $H_{ext} = 30$ mT applied in plane. c) Dispersion curves at different out-of-plane H_{eff} effective field values.

DOI:10.15774/PPKE.ITK.2018.003

Usually, in the literature there are three special geometries distinguished. In the normally magnetized film ($\psi = 0$) spin waves are called forward volume waves. In case of the tangentially magnetized film ($\psi = \pi/2$) there is a dependence on ϕ in Eq. 2.7 which means anisotropic wave propagation. The two special cases are referred to as backward volume waves ($\phi = 0$) and surface waves or alternatively Damon-Eshbach waves ($\phi = \pi/2$). The terms forward and backward refer to the relation between the phase velocity $v_p = \frac{\omega}{k}$ and group velocity $v_g = \frac{d\omega}{dk}$. In case of forward volume waves the phase velocity and group velocity vectors point to the same direction, even though they have different magnitudes. In the case of backward volume waves, for small k values (dipole dominated waves) the group velocity is negative and thus points to the opposite direction as the phase velocity. In case of volume waves, the wave amplitude is distributed sinusoidally across the volume of the film, while in case of surface waves the spin waves are localized to the surfaces of the film[18].

DOI:10.15774/PPKE.ITK.2018.003

Chapter 3

SPIN-WAVE COMPUTING PRIMITIVES

3.1 Introduction

This chapter shows a simple case study on how to re-invent optical computing primitives in a spin-wave medium. First we show the construction of coherent spin-wave sources and phase shifters in Section 3.2. These are the key components of a wave-based processing system. Lenses and mirrors are the most omnipresent components of an optical processing system, and Section 3.3 and 3.4 shows how spin-wave lenses and mirrors can be constructed.

3.2 Components for wave-based computing

3.2.1 Simulation setup

For proof of principle simulations, we used the well-established OOMMF code [15] with the *Oxs_SpinXferEvolve* module to include spin-transfer effects. A 5 nm thick Permalloy film was assumed with $M_s = 8.6 \cdot 10^5$ A/m, $A_{exch} = 1.3 \cdot 10^{-11}$ J/m and a damping constant of $\alpha = 0.008$. For calculating spin-transfer torque, we assumed $\Lambda = 1.5$, $P = 0.5$ and a polarizer layer pointing parallel to the film plane. For the interpretation of these parameters see the OOOMF manual [15]. The magnetic fields generated by the currents were not taken into account. We assumed $T = 0$ K temperature effectively ignoring temperature-induced decoherence of spin waves. To suppress domain formation in the film, a $B = 0.9$ T external field was applied in a 87° angle from the film plane, the resulting magnetization in the film is approximately 45° out-of-plane. (If the magnetic field was set to 90°, out-of-plane domain-walls formed in the film, and spin-waves scatter on these walls.) The field directions are shown in Fig. 3.1a) – the sketch also shows the expected precession orbit of the spin vector.

In all the simulations we applied spin-wave absorbing boundary conditions, by gradually increasing the value of the α damping constant from $\alpha = 0.008$ to $\alpha = 0.5$. Physically, this approximates a large (at least several micrometer size) magnetic film, where reflections from the boundary are negligible.

3.2.2 Spin-wave sources

In the simulations presented in this chapter we used nano-contact spin-torque oscillators (STOs) as spin-wave sources. STOs exploit the self oscillations of the magnetization driven by the spin-transfer torque of a current through the magnet. It is experimentally well-established that STOs generate coherent spin waves that propagate to large (several micrometers long) distance in Permalloy films [20]. STOs are point sources of radiation, which, according to the Huygens-Fresnel principle, can be used to create an arbitrary wavefront. Both

DOI:10.15774/PPKE.ITK.2018.003

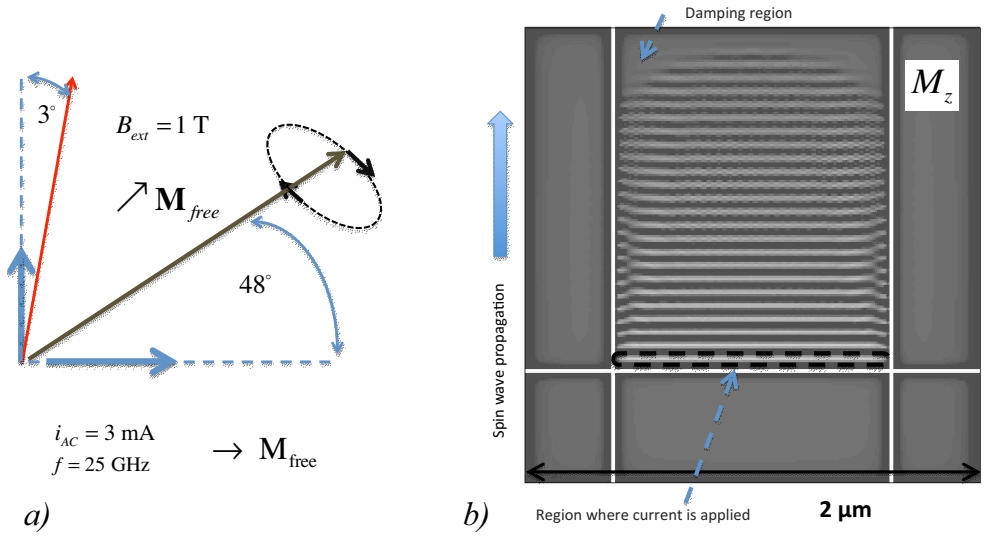

Figure 3.1. Panel *a*) shows the magnetization and field directions we used, and *b*) is a snapshot of the distribution of the out of plane magnetization component, M_z, showing the propagation of spin-wavefront.

the amplitude and phase of the point sources may be controlled. A plane wave can be created by a series of STOs, but the phase of the STOs must be kept constant in order for the wavefront to remain coherent. In order to achieve perfect phase coherence between the oscillators, we used an $i = 3$ mA, $f = 25$ GHz frequency AC current to drive them. In effect, the free magnetic layer will oscillate with this $f = 25$ GHz frequency and not by the natural oscillation frequency of the STO. The phase of the STOs will be identical and will follow the phase of the external AC signal. We are aware of the fact that it is a misnomer to call our spin-wave generating structures STOs, because the name 'STO' usually refers to autonomous oscillators driven by DC currents, and their phase is a free variable. The physical layer structure of these spin-wave generators is identical to the structure of an STO, but their oscillator dynamics is completely different.

Fig. 3.1b) shows a micromagnetic simulation of a spin wave generated by 64 individual, 30 nm diameter STOs. These generate a coherent plane-wave wavefront with $\lambda = 45$ nm wavelength, propagating upwards. Landau-Lifshitz damping noticeably decreases the amplitude of the spin waves, but at $d = 2$ μm distance from the STOs their amplitude remains close to the original value.

In the simulation of Fig. 3.1b) each STO receives identical current. However, for the proposed device application we assume that the driving current of the STOs can be individually controlled. Therefore the amplitude distribution of the spin-wave wavefront can represent an analog vector.

DOI:10.15774/PPKE.ITK.2018.003

3.2.3 Active damping

The Landau-Lifshitz-Gilbert-Slonczewski (LLGS) equation includes a spin torque term [21]:

$$\frac{d\vec{m}_f}{dt} = -\mu_0 \frac{|\gamma|}{1+\alpha^2} \vec{m}_f \times \vec{H}_{eff} - \alpha \frac{|\gamma|}{1+\alpha^2} \vec{m}_f \times \left(\vec{m}_f \times \vec{H}_{eff}\right) + \frac{g(\Theta_m)\mu_e I}{eM_s V} \vec{m}_f \times \left(\vec{m}_f \times \vec{m}_p\right)$$

If $\vec{m}_p$ is parallel to $\vec{H}_{eff}$ we can define:

$$\alpha_{eff} = \alpha \frac{|\gamma|\mu_0 H_{eff}}{1+\alpha^2} - \frac{g(\Theta_m)\mu_e I}{eM_s V}$$

Thus using negative DC current can increase the damping. We verified this by micromagnetic simulations. We estimate that to decrease the amplitude of a wave by an order of magnitude through a 20 nm wide region 3-5 mA current required, which is more, than what we use for generation (1 mA), but still a reasonable value.

3.2.4 Phase shifters

The operation of optical components (lenses, filters, diffraction gratings, etc.) is based on manipulating the phase and / or amplitude of the waves. The properties of the wave are changed by manipulating the index of refraction (n) of the medium through which the light propagates. The index of refraction can be defined for any other type of linear waves as $n_{21} = \frac{\lambda_1}{\lambda_2}$, where λ_1 is the wavelength in the first medium, and λ_2 in the second medium. The index of refraction is therefore straightforwardly defined for spin waves [22], [23].

Locally applied magnetic fields change the wavelength of the propagating spin wave. We numerically determined the $\lambda(B)$ relationship by simply applying a different B field in the upper area of Fig. 3.1b) and measuring the altered wavelength in this region. Figure 3.2 shows the wavelength vs. local field for this particular geometry. If the external field is the same $B = 1$ T is field that is applied at the spin wave source (at the STO), then $n = 1$ and the spin wave propagates undisturbed. Otherwise, n and λ shows a non-trivial dependence on the field.

3.3 Spin-wave lens

As a simple example, we construct the spin-wave equivalent of a convex optical lens. We (arbitrarily) choose to apply a $B = 1.6$ T field, which corresponds to an effective index of refraction $n \approx 0.6$. Since $n < 1$ for this B value, the field has to be applied in a concave shape in order to achieve a focusing effect. The curvature of the lens defines its focal length – and we in fact used a standard lens maker's equation to define the shape of the spin-wave lens. Figure 3.3 shows a micromagnetic simulation of a lens.

In the simulations, the lens is defined as an area with higher magnetic field and with an abrupt boundary, but this is a simplification. There are various ways in which the local mag-

DOI:10.15774/PPKE.ITK.2018.003

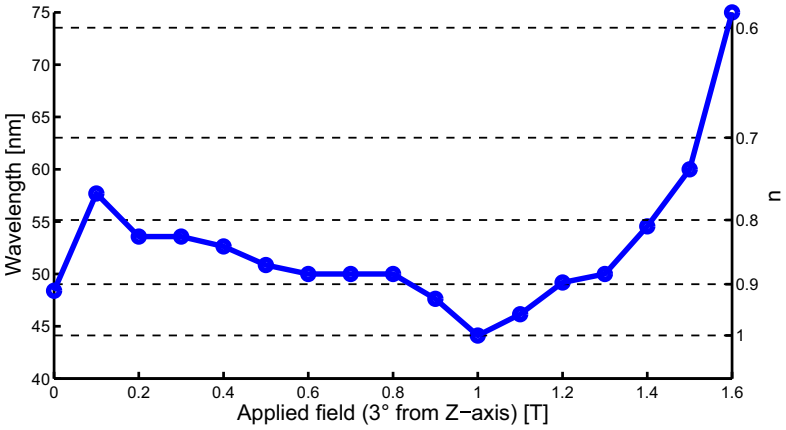

Figure 3.2. The dependence of the spin-wave wavelength on the applied magnetic field. An index of refraction can be assigned to the applied external field - it is given on the right axis.

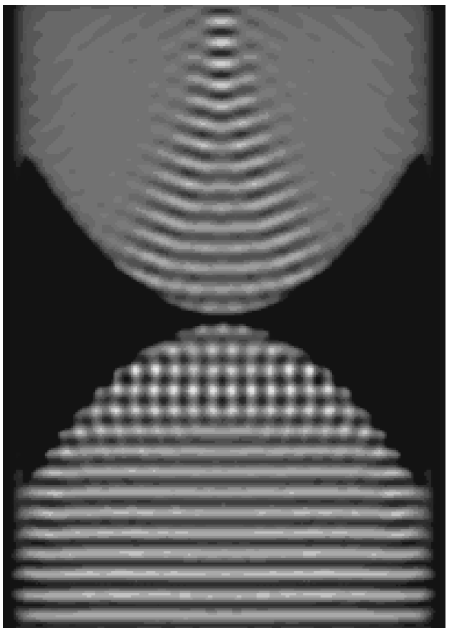

Figure 3.3. A micromagnetic simulation showing the focusing of a magnetic lens in a 1×1.5 μm Py film. The plane wave entering at the bottom is focused to one point at the top focal plane. The black concave lens shaped area is where the $B = 1.6$ T magnetic field is applied.

netic field may be realized. A locally higher magnetic field may be realized experimentally by a magnet placed on top of the film, which will generate a complex, non-uniform field distribution. These will change the transmission properties of the lens, so the shape of the lens has to be adjusted to correct it. Locally applied strain or spin-torque structures could realize a

DOI:10.15774/PPKE.ITK.2018.003

reconfigurable phase shifter – this can act as a lens with an adjustable focal length. Not only lenses, but diffraction gratings or more complex holographic filters can be defined using a similar hardware.

3.4 Spin-wave mirror

In general, spin-waves are reflected at boundaries of the magnetic material or by abrupt changes in material parameters or the magnetization. For this reason, convex and concave magnetic mirrors can be formed simply by shaping the bounding surfaces of the device. Since this is much simpler than applying large local magnetic fields, mirrors are easier to realize than lenses. They can be closer to be perfect, and have practically no losses.

3.5 Gradient-index lens

Similar to conventional gradient-index (GRIN) optics, we show that it is possible to construct a gradient-index lens for spin waves. Again, the index of refraction for spin-waves is set by an external magnetic field distribution here, since it is easy to do in simulations. However, the dispersion relation can also be changed by varying film thickness, or material parameters. In optics, a gradient index lens is used to focus light to a location outside of the lens, since it is usually not practical to detect light inside the lens. However, in case of spin waves it seems to be possible to place detectors inside the lens, thus we do not have such a limitation, and the length of the gradient index lens can be multiples of it's focal length. Such a construction might remind us more of a gradient index optical fiber, and the concept is the same, i.e., the gradient index guides the waves so that they follow a sinusoidal path and gets focused periodically. The different paths that rays take actually have the same optical length, even if physically the rays travel different distances. In the center, rays travel in a straight line in an optically denser material than those travel along an outer sinusoidal path. The gradient profile of a gradient index lens can be expressed as [24]:

$$n = n_0\left(1 - \frac{K}{2}r^2\right), \tag{3.1}$$

where n_0 denotes the index of refraction in the center of the lens (i.e. the most optically dense medium in the lens), K is called the gradient constant, and $p = \frac{2\pi}{\sqrt{K}}$ is called the pitch length (the length of one full sinusoidal path). Using the dispersion relation in the magnetic film and Eq. 3.1, the required magnetic field distribution can be calculated. Note, that the wavevector is proportional to the refractive index, instead Eq. 3.1, so we can write a similar formula for the wavevectors:

$$k = k_0\left(1 - \frac{K}{2}r^2\right). \tag{3.2}$$

Here k_0 denotes the wavevector in the center of the lens and it can be arbitrary chosen. However, since this corresponds to the lowest required external field value in the lens, it is best chosen as low as possible, just above the field required to saturate the magnetic film. Fig. 3.4 depicts the simulation results of a GRIN lens in an out-of-plane magnetized Py film. The

DOI:10.15774/PPKE.ITK.2018.003

wave focusing is much clearer than what we saw in the lens simulation, which suggest that lens aberrations and losses are much smaller in case of a GRIN lens. We can also observe, that the magnetic fields that are required are much smaller in most of the lens area than in the case of the geometrical lens, and there is no abrupt change in the required magnetization, which makes realization easier.

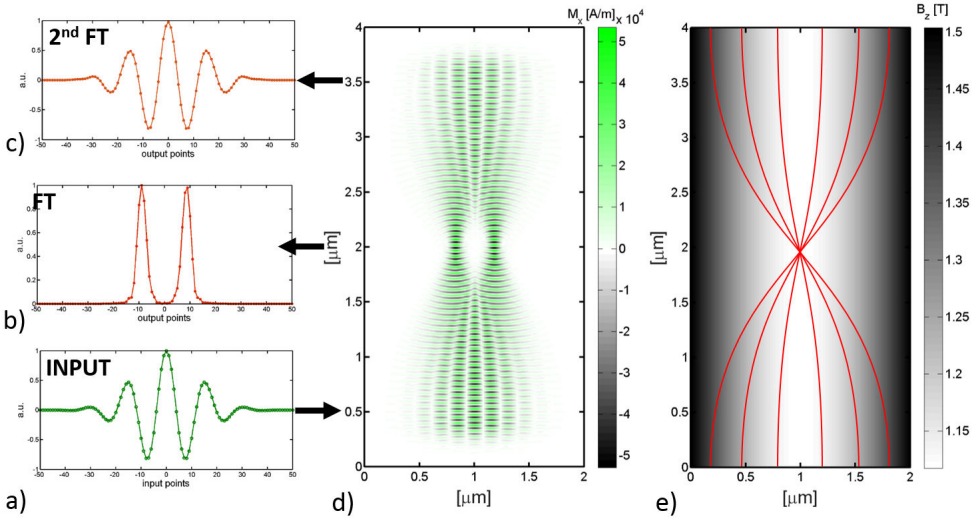

Figure 3.4. Gradient index lens

In a similar way, other parameters might be changed instead of the external field, and given that one know the relation between the wavevector and the graded parameter, it should be relatively straightforward to follow a similar path to design a lens. It is not in the scope of this work to physically design and experimentally demonstrate a GRIN lens, the exact realization of the lens gradient is left for further research.

3.6 Phase plates

Phase plates are thin regions that can shift the phase of the transmitted waves. This phase shift might be equal in every lateral position on the plate, or might be varying according to some function. There is a large number of transformations on the wavefront that can be realized using phase plates, and combinations (subsequent applications) of phase plates. Phase plates are a subset of filters, but phase plates does not alter the amplitude of the incoming wavefront, only the phase. Here, our goal is to show through an example how one might use phase plates in case of spin waves, and examine the benefits of doing so. We will show two

DOI:10.15774/PPKE.ITK.2018.003

functions that can be realized by phase plates and use them in combination in a micromagnetic simulation.

The first plate in the example is another way to realize a lens for spin waves. The phase plate shifts an incoming plane wave at every point by the required phase such that in the desired focal point all the waves interfere constructively. The phaseshift function can be chosen continuous along the plate, but alternatively might take values only in the $[0,\pi)$ interval. In our simulation we chose the later requirement to keep the maximum value of the locally applied external field as low as possible. The second plate in our simulation realizes an input pattern or a grating. This eliminates the need for spin-wave point sources, and the illumination can be realized by a plane wave, which might be generated e.g. by a waveguide or a spin-torque oscillator in an elongated shape. Here, we note that a phaseplate can either be static, or it might be actively driven by e.g. locally applied fields. This might be realized by spin currents through the film, or voltage controlled magnetoelectric cells. Alternatively a binary plate can be generated by nanomagnets on top of the film, which can be switched by a current (as in an MRAM cell).

The micromagnetic simulation results of the plates described above are depicted in Fig. 3.5. The Py film is magnetized out-of-plane and the external film distribution can be seen in Fig. 3.5a. The input plate and the phase plate with the lens functionality together form a Fourier transform, and the result can be read out in the focal plane of the lens.

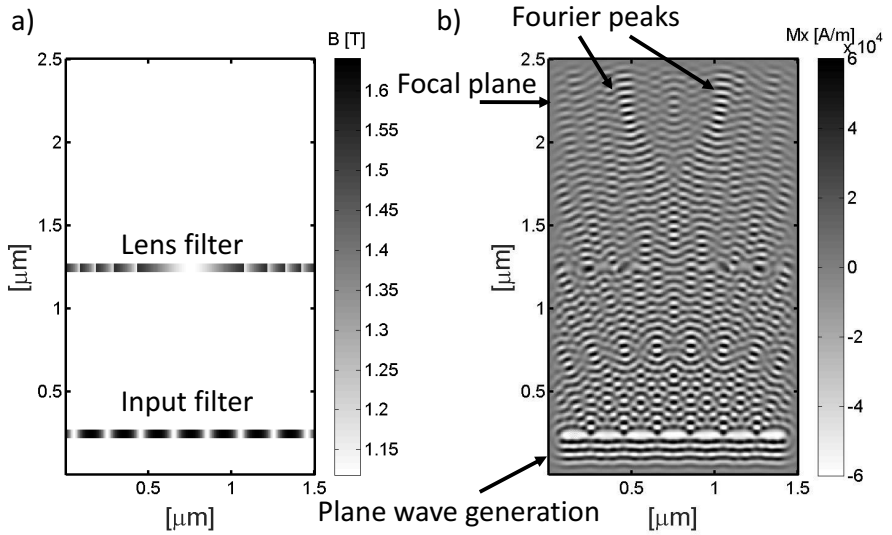

Figure 3.5. Fourier transform realized by two phase plates. a) Applied magnetic field. b) Simulation of phase plates to perform Fourier transform (magnetization snapshot).

DOI:10.15774/PPKE.ITK.2018.003

Chapter 4

DESIGN OF MAGNETIC WAVE COMPUTING DEVICES

4.1 Introduction

In the previous chapter, we demonstrated some basic optically-inspired spin-wave components, and here we demonstrate simple devices that can be built out of these components. The ideas can be borrowed from optics, but new designs have to be created for the magnetic media.

4.2 Spin-wave fourier transformation

4.2.1 Fourier transformation using a magnetic lens

A well-known and often exploited property of the optical lens is that it can perform a Fourier transformation. Here, we demonstrate using micromagnetic simulations that a spin-wave lens does the same. A simulation example is shown in Fig. 4.1. At the bottom of the simulation region, the input vector is defined by the driving currents of an STO array – for this example, the intensity distribution of the plane wave is chosen according to a Hann-windowed sine function. The windowing is used to suppress the side lobes that would arise because of the finite signal length. In the focal plane (at the top of the simulation region), the spin-wave amplitude distribution gives the Fourier transform of the applied input vector. Three peaks can be clearly recognized in the Fourier plane: the zero order (DC) component, and the two lateral lobes which correspond to the principal frequency component of the sine function.

To better understand the operation of the device, we may regard the STO sources as equivalent to Huygens' sources in a wavefront that passes through a grating with variable opacity. A sinusoidal grating will produce one frequency peak in the Fourier spectrum, while a rectangular grating with binary opacity will create higher order lobes after the wave passes through the lens. These lobes correspond to the Fourier series of a square wave. In order to correctly represent a signal, the density of the STO point sources has to meet the Nyquist criterion. On the other hand, according to the grating equation, the grating period can not be smaller than the spin-wave wavelength. This places a limitation on the maximum achievable resolution in a given device size and given spin-wave wavelength.

4.2.2 Fourier transformation using a mirror

Lenses can be replaced by parabolic mirrors if the geometry allows. The most important difference is that mirrors reverse the propagation direction of the wave. A mirror has several

DOI:10.15774/PPKE.ITK.2018.003

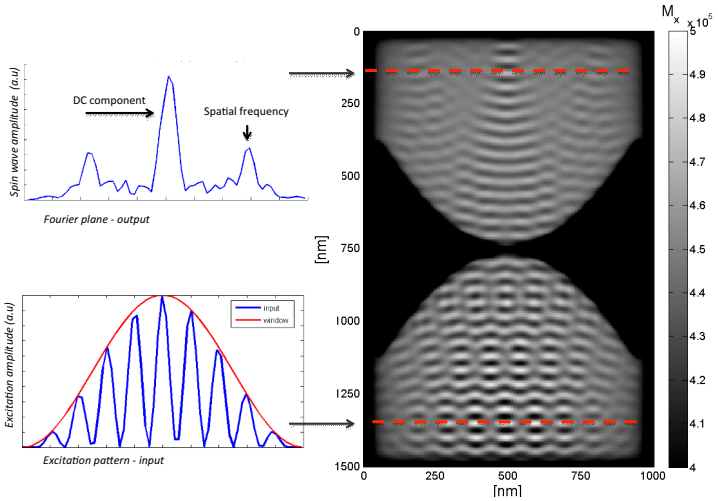

Figure 4.1. A micromagnetic simulation showing the Fourier transform property of a spin-wave lens. The input wave pattern enters at the bottom. The black area is where a $B = 1.6$ T magnetic field is applied. The Fourier transform of the input vector appears as the intensity distribution in the focal plane, at the top of the simulation region.

advantages compared to fabricating a lens, (i) it is fabricated at the edges of the magnetic film rather than inside or on top of the film, (ii) there are only minor reflection losses at the surface, and (iii) there is no limit for the focal distance as in the case of lenses due to the limited refractive index.

We designed a spin-wave device that performs a Fourier transformation using a parabolic mirror. The focal distance is set by the curvature of the parabola. The focal distance is an important design parameter: if too short, the far field approximation is no longer true, on the other hand, if it is too long, the readout signal will be very small due to spin-wave decay. Fig. 4.2 illustrates the chosen geometry of the spin-wave mirror and demonstrates how it performs a Fourier transform on an incoming wavefront. Fig. 4.2a,b show the spin-wave amplitude in the magnetic film. Absorbing boundary conditions are applied on all sides of the simulation region, except on top (by the mirror).

The input in this example consists of a line source of 91 oscillators, and the device performs a Fourier transformation on the 91-element analog vector, as indicated in Fig. 4.2. The wavefront propagates from the input sources in the focal plane to the mirror, reflects back, and form the output waveform in the same focal plane.

A drawback of using a mirror is that the readout must be performed at the same position where the inputs were applied. Time multiplexing can be used to separate input and output, i.e. first we turn on the sources, and generate the wave for a certain time (e.g. the time it takes to the spin-waves to take the focal distance twice), and after that we stop generating, and start reading out. After all the waves reflected back and reached the focal plane or the boundaries we can apply a new input. The reflected waves can be read using the same oscillators that created the waves or other type structures can be placed in close proximity to the input line.

DOI:10.15774/PPKE.ITK.2018.003

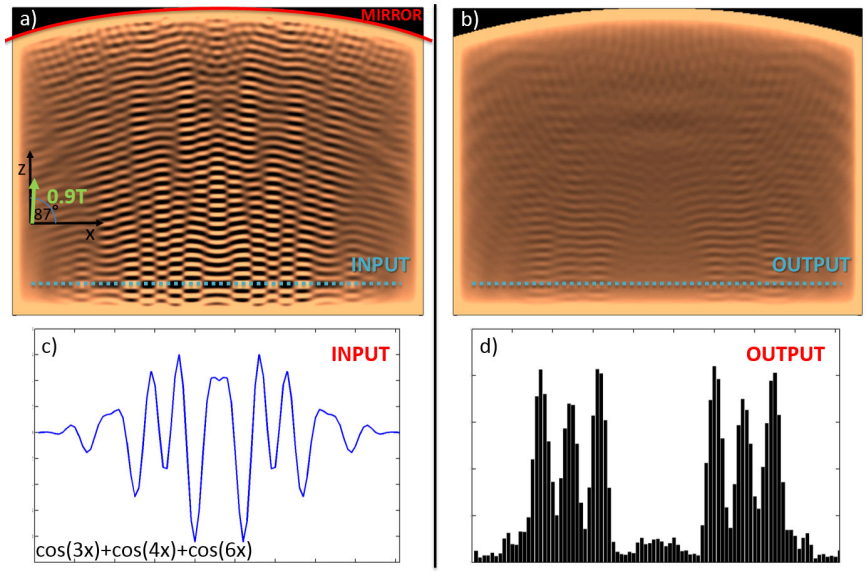

Figure 4.2. Fourier transformation by a parabolic mirror a) the magnetization of a 2 μm x 1.5 μm film after applying the input b) the magnetization of the film during readout c) the input function d) the amplitude of the waves in the output line

For clarification, the device performs Fourier transformation on input sources organized in space, so the result is an array of spatial frequency components. However, the spin-waves traveling inside the film have a frequency distribution in time, due to the non-perfectly monochromatic sources and other noise sources. We will refer to these as temporal frequency components.

4.2.3 Double mirror

In order to realize more complex operations, at least two mirrors are necessary. However, unlike in the case of lenses, at most two parabolic mirrors might be arranged coaxially (in case of paraxial approximation). In order to perform subsequent Fourier transforms, two parabolic mirrors can be placed facing each other with coinciding focal planes. Fig. 4.3 shows this two-mirror arrangement, which performs a Fourier / inverse Fourier transformation. The figure shows three snapshots of the operation: The waves propagate in both directions from the source (Fig. 4.3a), reflect from both mirrors (Fig. 4.3b), then cross the focal plane, reach the other mirror and reflect again (Fig. 4.3c).

After the second Fourier transformation, the original signal should reappear at the output. Fig. 4.3d shows the input and output waveform after the second Fourier transformation. The good match demonstrates the device works as expected.

Clearly, a Fourier / inverse Fourier transform alone is of limited use. However, if a filter is placed in the Fourier plane, then this arrangement performs frequency-domain signal processing operations, which are universally used in electronics. Such filters may be realized by locally applied magnetic fields, or interaction with spin-torque current. A simulation of

DOI:10.15774/PPKE.ITK.2018.003

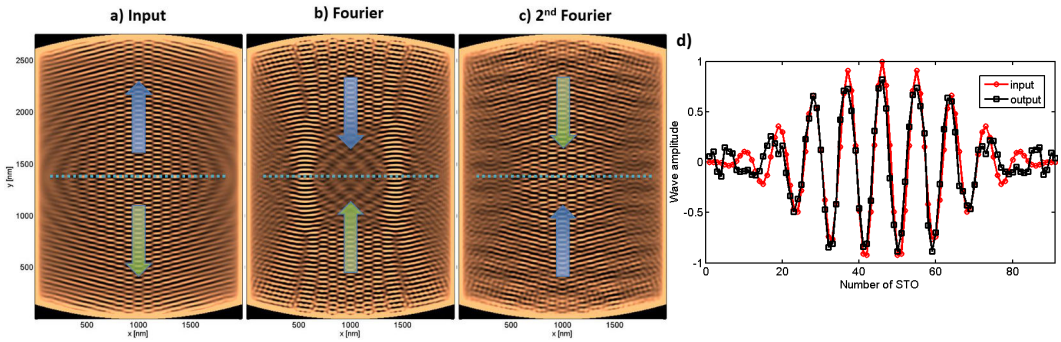

Figure 4.3. The operation of the double mirror device (snapshots of the magnetization) a) the forward propagating waves from the input line in two direction b) the reflected waves from the mirrors c) after the second reflection the original waveform appears. d) The input and the second Fourier transformation provided by the double mirror device. The amplitudes are scaled to the same power level.

such a device is shown in Figure 4.4. The filter is applied dynamically in time in the second phase of the operation, when the waves reflect back from the mirrors and form the Fourier transformation of the input signal. The filtering here is realized by active spin-torque current structures operated in damping mode.

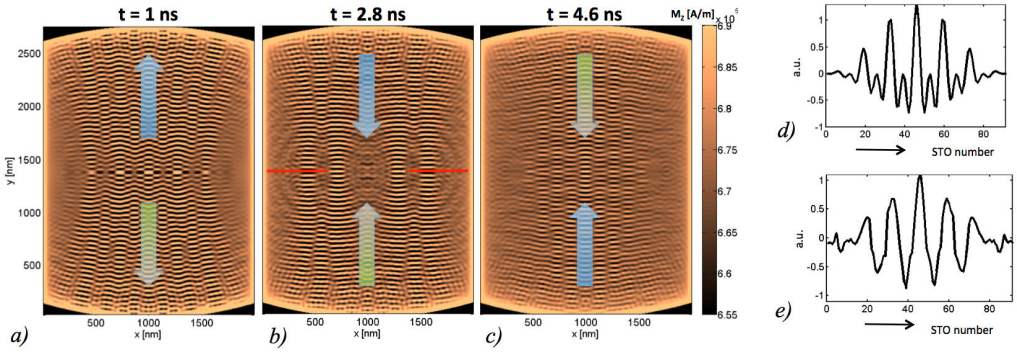

Figure 4.4. Fourier domain filtering using the double-mirror setup. a) Generation and propagation of spin waves. b) Absorbing filter applied when reflected waves reach focal plane. c) Filtered wave arrives focal plane – readout. d) Input pattern. e) Output (filtered) pattern.

DOI:10.15774/PPKE.ITK.2018.003

4.2.4 Performance considerations

Since in the double-mirror system, the waves should travel to the mirror and back at least twice, damping can be a serious issue. Fig. 4.5 shows that geometrical losses (waves leaving at sidewalls) lower the total energy approximately by a factor of 4 in a cycle. Also, the Permalloy damping causes losses in the same order of magnitude. In simulations the design presented here gives similar results if we use, except the output amplitude (and thus the SNR – Signal to Noise Ratio) is much more reasonable, about one or two orders of magnitude higher. In simulations the two mirrors are placed perfectly symmetric to the focal plane, so the waves which reflect from the two mirrors interfere in the focal plane perfectly constructively. However, fabrication variations might cause the interference to be destructive, if one of the mirrors is off by approximately half the wavelength. Thus, fabrication tolerances are required to be at least an order of magnitude lower than the wavelength.

Fig. 4.5a shows the magnetization of the film in the focal plane in time (i.e. the output waveform) for a plane wave. In the first 1.6 ns, the sources are generating waves. After that, for 1.6 ns the sources are turned off. The Fourier transformation of the plane wave (a peak at the center) appears in the second period. Note, that there is another, lower frequency component besides the expected output, this is probably caused by self oscillations of the film due to the abrupt stop of the signal sources. This temporal frequency component is well separable, and has to be filtered out to get the correct output. In Fig. 4.2d and Fig. 4.3d we show the results with this component already removed.

Fig. 4.5b shows results to estimate the power flow in the spin-wave mirror device. According to our simulations, a 91 point Fourier transform can be performed in 3.25 ns and dissipating 2500 eV magnetic energy (from Fig. 4.5b). This corresponds to a performance of 28 GS/s at 0.12 μW. Comparing to a highly optimized state of the art CMOS FFT chip with 1024 point 240 MS/s at 3 mW [25], and upscaling the spin-wave device for fair comparison to 1024 point, 2.5 GS/s at 1.3 μW, we gain an order of magnitude in speed and three orders of magnitude in power consumption. It shows that for certain applications spin-wave-based computing devices may have a significant benefit as compared to conventional CMOS technology.

These calculations show only intrinsic losses in the magnetic film. The net power consumption of the circuit, which takes into account losses in the CMOS supporting circuitry and the losses in the magnetic/electric interface, will be significantly larger. Still, these numbers show that the device has the potential to achieve orders of magnitude power efficiency improvement over CMOS in certain special applications.

4.3 Conclusions

We took a step toward wave computing devices realized by spin-wave propagation in magnetic media. Our simulations serve as a case study using well known concepts and algorithms to provide evidence of the potential of using spin-waves for realizing wave computing algorithms. The presented device can perform Fourier transformation and filtering on low to medium number of element analog vectors with low accuracy, with an order of magnitude

DOI:10.15774/PPKE.ITK.2018.003

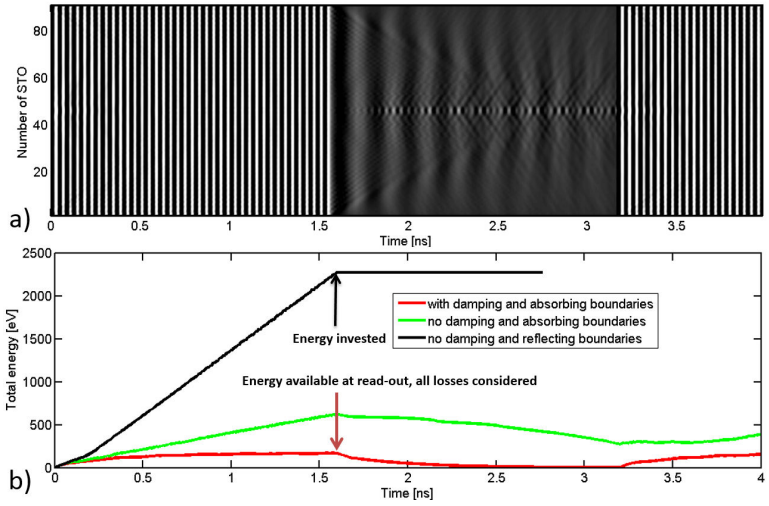

Figure 4.5. a) The output of the 91 oscillator in time b) the energy of the magnetic film in time. The black curve shows the total energy invested by the oscillators (without losses), the green curve shows the available energy in the film without damping (only boundary losses), the red curve shows the energy considering both damping ($\alpha = 0.008$) and boundary losses.

higher speed and up to three orders of magnitudes lower power consumption than conventional CMOS circuits.

We believe that this technology can be suitable to realize more complex algorithms like wave-based correlators, matched filters or holographic algorithms. A hardware accelerator that can perform these basic algorithms fast and energy efficiently can significantly improve other general purpose signal processing systems.

DOI:10.15774/PPKE.ITK.2018.003

Chapter 5

A SPECTRUM ANALYZER DESIGN BASED ON THE ROWLAND CIRCLE[1]

5.1 Introduction

We present the design of a spin-wave-based microwave signal processing device. The microwave signal is first converted into spin-wave excitations, which propagate in a patterned magnetic thin-film. An interference pattern is formed in the film and its intensity distribution at appropriate read-out locations gives the spectral decomposition of the signal. We use analytic calculations and micromagnetic simulations to verify and to analyze the operation of the device. The results suggest that all performance figures of this magnetoelectric device at room temperature (speed, area, power consumption) are potentially order(s) of magnitude better than what is achievable in a purely electrical system. We envision that a new class of low-power, high-speed, special-purpose signal processors can be realized by spin-waves.

Magnetic excitations (spin waves) are one of the most promising 'alternate state variables' in electronics, due to their potentially very low energy, short wavelength, and high speed. A number of proposals and/or device demonstrations use spin waves for realizing Boolean logic gates [27] or non-Boolean computing primitives [28],[29]. In this chapter, we present a new class of devices and also a new application area for spin-waves. In particular, we show that they are very well-suited for high-frequency and extremely compact spectrum analyzer devices. Our device also exemplifies how ideas from non-Boolean, optical devices can be re-invented in the domain of spin-waves, which could be much more amenable to integration than light waves.

In the studied device, the microwave signal first is converted into spin-wave excitations. The magnetic field of a simple waveguide can generate a coherent spin-wave wavefront in a magnetic thin-film. The signal processing takes place in the spin-wave domain, via interference, and the resulting interference pattern is picked up electrically at the output. The schematics of the spin-wave based processor is shown in Fig. 5.1. The wavelength of the studied spin-waves is two to six orders of magnitude shorter than the microwave wavelength at the same frequency, so switching to the spin-wave domain could enable very compact devices. The spin-wave wavefront carries energy that is about three orders of magnitude less than the energy of the generating microwave signal, giving the potential of very low-energy processing. Spin-wave signals do not suffer from parasitic capacitive or inductive couplings, and the low magnetic damping of ferrite thin-films [30] allows high signal integrity. The spectral analysis is done by spin-wave interference pattern formation. In effect, the interference pattern on the patterned film is functionally equivalent to a filter bank, made of high-Q factor LC components.

[1] The results presented in this chapter corresponds largely to [26]

DOI:10.15774/PPKE.ITK.2018.003

Microwave spectrum analysis is an essential capability in today's telecommunications and electronic warfare systems, and also in many data processing applications. Due to the relatively long wavelength of microwave signals (centimeter range) and due to the fact that it is challenging to fabricate high-quality on-chip inductors and filters at higher frequencies, it remains challenging to fabricate fast, power efficient and high-resolution spectrum analyzers in a compact size. Digital spectrum analyzers can be made much more compact then passive ones, but they require high-speed analog-digital converters (ADCs), and such ADCs consume several watts of DC power. Frequency-domain processors, MEMS-based systems face similar challenges.

It must be noted that an on-chip, interference-based processor was recently proposed by Afshari et al. [31] – this work actually uses lumped *LC* elements to perform spectral analysis. However, due to the relatively large serial (parasitic) resistance of the inductors, this device is hard to scale to large sizes and consumes significant power. Here, we will argue that spin-waves may perform better in this aspect as well.

The use of magnetic materials in microwave signal processing and spectrum analyzers is not new. Magnetically tunable high quality oscillators can be made out of YIG (yttrium-iron-garnet) spheres with size under a millimeter [32]. Using YIG, filter banks and channelizers can be built, and exploiting the nonlinear property of the magnetic waves, frequency selective limiters have been demonstrated. Circulators and isolators typically use ferrites such as YIG. These devices, however, do not use magnetic excitations to actually carry information – rather, they use the magnetic materials as tunable permeabilities, exploiting the interaction of guided waves and magnetic excitations. A notable exception is the patent by Hanna et al. [33], where beams of magnetic waves are deflected by a flat grating created by surface acoustic waves – we are not aware of any follow-up on this idea.

We believe that the only significant challenge in realizing these proposed type of magnetoelectric devices is the conversion of spin-wave signals back into the electric domain, which is required for most real-life applications. Due to the low energy and high frequency of the spin-waves, one needs fast, low-noise amplifiers for the magneto-electric conversion. Despite this challenge, spin-wave devices have the potential to combine ultra-low power and high-frequency operation, which is a virtually unmatched property among electronic/nanoelectronic devices.

5.2 Principles for wave-based spectral analysis

At the heart of the proposed device is a concave grating, that serves dual purpose: 1) it creates a diffraction pattern and 2) it focuses the waves. Concave gratings are traditionally used in optical and x-ray spectroscopy, typically in Rowland circle spectrographs [34], [35]. Concave gratings offer several advantages over conventional flat gratings by eliminating the need for lenses in the system – lenses are often difficult to realize outside the optical domain.

A schematic sketch of a generic Rowland circle spectrograph is shown in Fig. 5.2. At the bottom of the device is the curved grating. This diffracts waves with different wavelengths along different directions, and – due to its concave shape – also focuses them to different points on the Rowland circle, as indicated in Fig. 5.2. Since the wavelength depends on the

DOI:10.15774/PPKE.ITK.2018.003

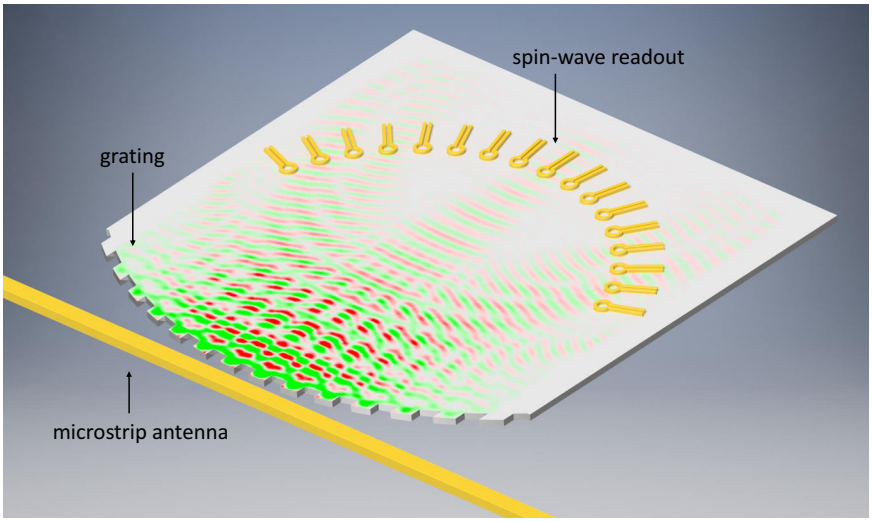

Figure 5.1. Schematic layout of the proposed spin-wave-based spectrum analyzer. The input signal is injected into a microstrip antenna, which generates spin waves on the patterned edge of an adjacent magnetic film. The interference pattern created by the spin waves is read out at specific locations using nanoscale loop antennas. The interference pattern is created in a way so that the frequency components of the input signal will become separated spatially.

excitation frequency, different frequency constituents of a time-domain signal will launch waves with different wavelengths. So if a signal with multiple time-domain spectral components is launched from the grating, then the intensity distribution along the Rowland circle will give the spectral decomposition of that signal.

The spectral resolution of the device depends on the spatial separation of the spectral components on the Rowland circle. The deflection angle α (as seen in Fig. 5.3a) of a wave with wavelength λ on a grating with grating constant d is given by the grating equation [34]:

$$\sin\alpha = \frac{n\lambda}{d} \tag{5.1}$$

where n is the diffraction order. This formula is valid for flat gratings and a good approximation for gratings with small curvature, which is the case we consider here. In case of a concave grating, the deflection angle α is the same at every point on the grating and the waves with same wavelength are focused to a single point P on the Rowland circle (see Fig. 5.3a). It is easy to see that $\angle PCO = 2\alpha$ so the length of the arc is:

$$\widehat{PO} = 2R\arcsin\frac{n\lambda}{d}. \tag{5.2}$$

Thus, for small angles, the position of the focal point P on the Rowland circle depends approximately linearly on the wavelength λ. The resolution of the system can be engineered by choosing the appropriate Rowland circle radius, R. Note, that any wave with a wavelength $\lambda \geq d$ will have only the trivial zero order component.

DOI:10.15774/PPKE.ITK.2018.003

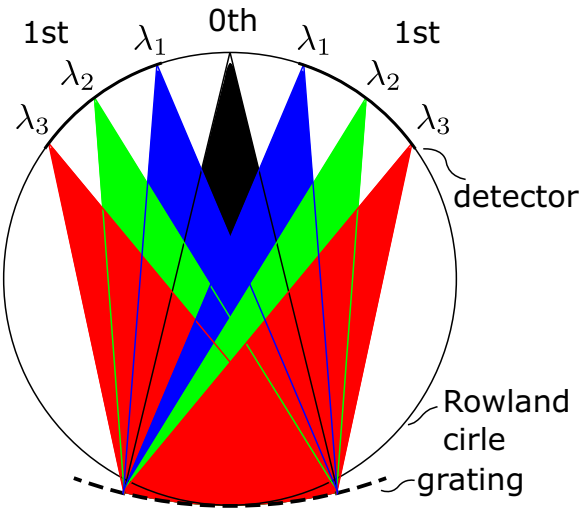

Figure 5.2. Schematic layout of a Rowland spectrograph. A multispectral time-domain signal excites waves at the grating, and the wavefronts interfere in such a way that the spectral decomposition of the signal appears as interference maxima on the Rowland circle.

Figure 5.3b) illustrates the location of the higher-order peaks. In the design of the spectrum analyzer, care must be taken to avoid overlap between different diffraction orders and this limits the operation of the device to a frequency band between the corresponding λ_{min} and λ_{max} wavelengths. For correct operation the input signal can not contain high frequency components with spin-wave wavelength less than λ_{min}, thus the input signal must be pre-processed (or post-processed) by a low-pass filter. The lowest frequency that can be distinguished without second order overlap corresponds to $\lambda_{max} = 2\lambda_{min}$.

The calculations presented so far use only the wavelength and assume generic linear wave properties. One needs to know the dispersion relation (wavelength-frequency relation) in order to determine the spectrometer resolution in terms of frequency. For electromagnetic waves, there is usually a linear relation between wavelength and frequency, while spin waves have a more complex, nonlinear dispersion relation.

5.3 Spin-wave propagation in magnetic thin films

Magnetic materials can be thought of as an assembly of interacting, elementary magnetic moments (spins). In a classical picture, a space and time-dependent, continuous magnetization distribution $\mathbf{M}(\mathbf{r},\mathbf{t})$ characterizes a ferromagnetic (or ferrimagnetic) material [18]. The spins are coupled to each other via magnetostatic and exchange interaction. Disturbances in the magnetization distribution propagate in a wave-like manner and are referred to as spin waves or magnons. For small amplitudes (few degree deflection of the $\mathbf{M}$ vector) spin waves behave as linear waves to a good approximation.

There are also major differences between spin waves and electromagnetic waves. The spin-wave dispersion relation strongly depends on material parameters and externally ap-

DOI:10.15774/PPKE.ITK.2018.003

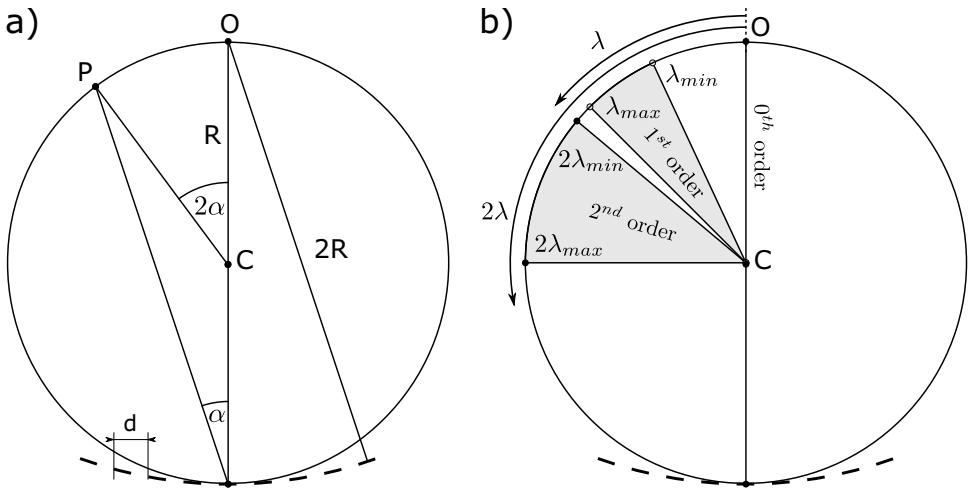

Figure 5.3. a) Sketch for calculating the resolution of the Rowland circle arrangement b) Position of the diffraction orders around the Rowland circle. λ_{min} and λ_{max} are the minimal and maximal wavelength components in the input signal. In order to avoid band overlap, $\lambda_{max} < 2\lambda_{min}$ must be fulfilled.

plied magnetic fields and may be 'engineered' by an appropriate choice of these parameters. Spin-wave wavelengths as small as a few-ten nanometers may correspond to microwave frequencies (5-100 GHz). Spin-wave propagation is often anisotropic and the wavelength depends on the relative orientation of **M** magnetization and the **k** wavevector. Spin waves are strongly damped in most ferromagnetic metals, but they may propagate large distances (thousand times wavelength) in ferrites (such as yttrium iron garnet, YIG) [17].

Spin-wave dynamics can be modeled by standard micromagnetic theory and a number of established software packages are available for this task [15]. Most of these simulators solve the Landau-Lifshitz-(Gilbert) equations (LLG equations) in the time-domain. For certain spin-wave propagation modes and certain parameters one can often linearize the LLG equations and/or find analytical solutions for the dispersion relation [36].

As an example, we consider dispersion relation for spin waves in a magnet that is magnetized along the $\hat{\mathbf{z}}$ direction [18]:

$$\omega = \sqrt{\left(\omega_0 + \omega_M \lambda_{ex} k^2\right)\left(\omega_0 + \omega_M \left(\lambda_{ex} k^2 + \sin^2\theta\right)\right)} \tag{5.3}$$

where $\omega_0 = \gamma\mu_0 H_0$, $\omega_M = \gamma\mu_0 M_S$, $\lambda_{ex} = \frac{2A_{exch}}{\mu_0 M_S^2}$, γ is the gyromagnetic ratio, μ_0 is the vacuum permeability, M_S is the saturation magnetization, H_0 is the total internal field, A_{exch} is the exchange coefficient, k is the wavenumber and θ is the angle between the propagation direction and $\hat{\mathbf{z}}$.

One may distinguish between two fundamentally different propagation modes of spin waves. For waves with large k (short wavelength), the term $\lambda_{ex} k^2$ in Eq. 5.3 is much smaller than one and is negligible compared to the other terms. Waves in this parameter regime are called exchange waves because the dominant interaction mechanism between oscillating spins is the exchange interaction. On the other hand, if $\lambda_{ex} k^2 \gg 1$ (long wavelength), then

DOI:10.15774/PPKE.ITK.2018.003

the dipole interactions dominate, and such waves are called dipole spin waves or magnetostatic waves. Exchange-waves have several orders of magnitude shorter wavelengths compared to electromagnetic (EM) waves at the same frequency, but even magnetostatic wave wavelengths are at least two orders of magnitude shorter than EM wave wavelengths. This makes spin waves attractive to use in compact (on-chip) applications.

The operation of the device proposed here relies only on the interference of linear waves and the device may be designed to work either in the exchange-dominated or the dipole-dominated spin-wave regime. Both modes of operation have benefits and drawbacks. Exchange waves allow much more compact devices, but make device fabrication and detection of spin waves more challenging. The benefit of short wavelengths is that if the size of the entire device is smaller than the electromagnetic wavelength then one does not need to worry about possible phase delays occurring in the microwave circuitry. It is worthwhile to mention that passive microwave components (filters, spectrum analyzers, surface acoustic wave devices, etc.) are rather large by the standards of microelectronics [37]. So, even if one assumes relatively long spin wave wavelengths (on the order of micrometers or more), this will still result in a device that is compact compared to most electrical implementations.

The dispersion relation of Eq. 5.3 depends on the angle (θ) between the direction of wave propagation and the magnetization. This dependence results in anisotropic wave propagation for in-plane magnetized films, but not in out-of-plane films, since in that case the out-of-plane (normal) vector is perpendicular to every wavevectors in plane. In the following we assume out-of-plane magnetized films in order to avoid complications that arise from anisotropic propagation.

In the previous section, we showed that in the Rowland configuration there is an approximately linear mapping between wavelength and the location of the corresponding focus point on the Rowland circle (Eq 5.2). In order to determine the mapping of frequencies, Fig. 5.4 shows calculated dispersion curves in a thin YIG film at various B_{ext} external fields. It is possible to set B_{ext} such that the frequency band of interest falls on a higher or lower slope of the dispersion curve. By doing so, one may achieve a narrow-band spectrometer with high frequency resolution, or wide-band spectrometer with lower frequency resolution while other design parameters remain unchanged.

As a concrete example, we assume $d = 4$ μm and $R = 1$ mm. The first order peak of a $\lambda_1 = 1$ μm spin wave will be focused at $\widehat{P_1O} = 505.4$ μm. The wavelength of a wave focused in the next output point at $\widehat{P_2O} = 501.4$ μm will have a wavelength $\lambda_2 = 0.992$ μm. If a bias field $B_{ext} = 300$ mT were applied, these wavelengths correspond to $f_1 = 5.465$ GHz and $f_2 = 5.466$ GHz, i.e. a frequency resolution $\Delta f = 1$ MHz corresponds to a $l = 4$ μm distance on the Rowland circle.

Magnetic damping will limit the spin-wave propagation length and diminish signal integrity. YIG has one of the lowest damping among known magnetic materials, with damping coefficient as low as $\alpha = 8.58 \times 10^{-5}$ for thin films[30] and decay lengths of up to thousand wavelengths [17]. The device in the above numerical example is realizable with reasonably strong spin-wave signal reaching the Rowland circle.

DOI:10.15774/PPKE.ITK.2018.003

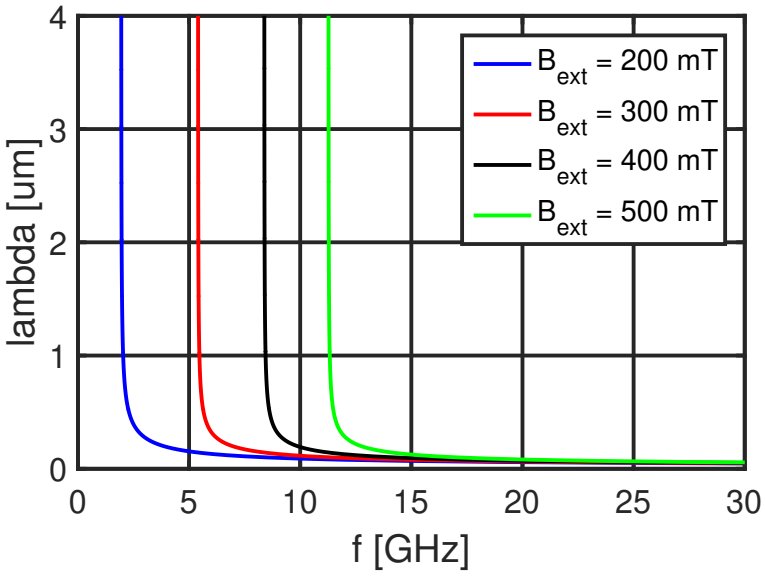

Figure 5.4. Calculated dispersion relation of spin waves in an out-of-plane magnetized YIG thin film assuming various external fields.

5.4 Generation of spin waves on a grating

In a conventional Rowland-circle spectrograph, an optical or x-ray beam is directed to the grating, which acts as a secondary source of waves. In the case of spin waves, the grating can be made the primary source of the spin waves.

The edge of a magnetic film, with a microstrip line running next to it, can act as the source of spin waves. The geometry is illustrated in Fig. 5.5a. The magnetic field generated by the current that runs through the microstrip line generates spin waves at the edge of the film.

The use of coplanar or microstrip waveguides for the generation of spin waves is well-established [38]. The magnetic field of such waveguides, is not well-localized. Waveguides are rather inefficient in creating spin waves with wavelengths that are smaller (or comparable) to their width. However, at the edge of a magnetic film, the demagnetization field changes abruptly. It is the net magnetic field (which is the superposition of demagnetization field, waveguide-generated magnetic field and other effective field components) that is responsible for the generation of the spin waves. We found that the abruptly-changing field at the edge of the waveguide is a significantly more efficient coherent source of spin waves than the waveguide alone.

Generating spin waves at and by the boundary of the magnetic film has another significant benefit: it enables precise phase-shifting of the waves by patterning the edge. A diffraction grating for micrometer-wavelength spin waves is able to introduce an initial phase shift at the spin-wave generation. This shift can be a few nanometers distance by appropriately patterning the boundary of the magnetic film.

An example of the phase-shifting edge is shown in Fig. 5.5b. The $h = 270$ nm step was designed to introduce an initial phase difference of $\phi = \pi$. The width of the waveguide in this

DOI:10.15774/PPKE.ITK.2018.003

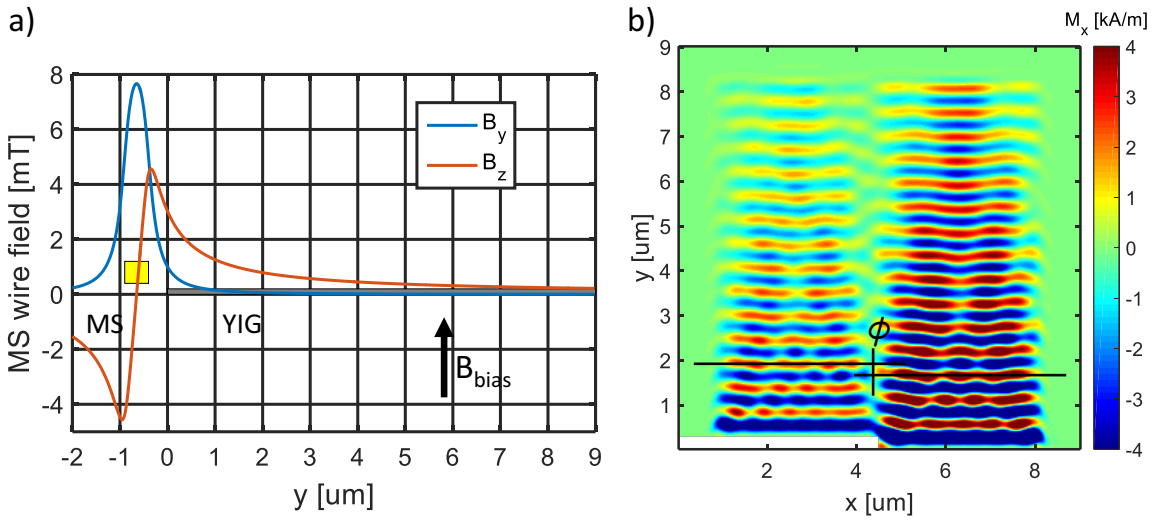

Figure 5.5. Spin-wave generation on the edge of a YIG film by a microstrip line (MS). a) Magnetic field of MS and schematics of arrangement. b) Time snapshot of the magnetization of YIG showing spin waves generated on the edge close to the MS (bottom). By patterning the film edge phase shifts may be introduced to the coherent wavefront.

example is $w = 500$ nm and its calculated magnetic field is depicted in Fig. 5.5a. The magnetic field of the MS line was calculated numerically by integrating the field components generated by small sections of the MS wire using Amperes law. In this simplified simulation model, we assumed uniform current distribution and neglected the effect of the ground plane and the dielectric. The calculated field is concentrated around the MS wire, where the magnetic film edge is located. Consequently, the magnetic film edge experiences almost exactly the same field at the two sections of the step, but in one side the source is shifted by the h step size resulting in a phase shift.

A periodic structure built from the steps of Fig. 5.5b, next to the waveguide, can simultaneously act as the spin-wave source and diffraction grating in a spin-wave-based Rowland circle. The wavefront generated on the edge of the film will be equivalent to a wavefront created by illuminating a binary phase grating with a plane wave. A single frequency microwave input will produce multiple order peaks with relative amplitudes given by the Fourier series of the grating ruling shape. It is important to note, that a patterned edge acts primarily as a phase modulator, so a sinusoidal grating pattern will not produce a single peak, as it would be expected from a sinusoidal amplitude grating. Instead, the relative amplitude of the peaks is given by Bessel functions of the peak-to-peak phase delay of the grating [39]. In the case of phase gratings it is not possible to design a grating that is single order in case of all the wavelengths, since the amount of phase shift depends on the wavelength as well.

DOI:10.15774/PPKE.ITK.2018.003

5.5 Micromagnetic simulation of the spectrum analyzer

We used micromagnetic simulations (OOMMF [15]) to verify and demonstrate the design above. OOMMF solves the Landau-Lifshitz-Gilbert equations in the time domain. This approach is based on the fundamental equations of micromagnetics and avoids most approximations – but is computationally intensive. For two-dimensional structures typically a few micrometer by few micrometer size structure is reasonable to simulate.

We simulated a 10 nm thick YIG film with saturation magnetization $M_s = 1.4 \times 10^5$ A/m, exchange constant $A_{exch} = 3.65 \times 10^{-12}$ J/m and $\alpha = 0.001$ damping constant. This damping constant is much higher than what is achievable in state of art YIG thin films, but we assumed a pessimistic value and the larger damping constant also made the numerical calculation more stable. We chose a lateral cell size of 15 nm – while this is a relatively coarse discretization, it allows the simulation of a 15×15 μm area on an average workstation and within a few days of simulation time. In order to verify the accuracy of the used cell size, we performed simulations on similar structures using much finer discretization (all the way down to 5 nm) and on much coarser grids, and the simulations gave nearly identical results as long as the cell size was small compared to the spin wave wavelength studied. The out-of-plane external bias field was set to $B_{bias} = 520$ mT, which according to the dispersion relation corresponds to a wavelength of $\lambda \approx 525$ nm at a frequency $f = 10$ GHz.

The geometry of the magnetic film follows the design described above: at the bottom of the structure there is the curved grating, serving also as the source of spin waves. This edge of the YIG film was patterned in a cogged shape on an arc with a radius of $2R = 12$ μm, where R is the Rowland circle radius. The grating constant was set to be equal to double the wavelength $d = 2\lambda$ at 10 GHz and the height of the cogs is $h = \lambda/2$, which equals a phase shift of π.

The input signal, which is the magnetic field of the waveguide, appears in the simulation as a time varying external magnetic field. In the present example, this field is a superposition of two sinusoidally varying magnetic fields at $f_1 = 10$ GHz and $f_2 = 10.25$ GHz. The field distribution of the waveguide was calculated numerically in an independent simulation as described previously, assuming a microstrip line with width $w_{ms} = 500$ nm, thickness $t_{ms} = 200$ nm and dielectric thickness $t_{diel} = 100$ nm. The microstrip was placed 400 nm from the YIG film. The microwave current amplitude in the line for both frequency components was 0.5 mA. We calculated the the current distribution and the waveguide magnetic field using HFSS a full-wave electromagnetic simulator. We ignored the influence of the magnetized film on the waveguide.

On the other three edges of the YIG film absorbing boundary conditions were realized by a linearly increasing damping coefficient in a 1500 nm region up to a maximum damping coefficient $\alpha = 0.5$. This boundary condition eliminates most reflections from these edges, effectively simulating an infinitely extended film in these directions.

The simulation was performed in two steps: in an initial simulation only the bias magnetic field was applied, without the oscillating field component and the damping constant was set to $\alpha = 0.5$ everywhere. With the artificially high damping constant, the simulation quickly converges to a steady-state $\mathbf{M}(r)$ magnetization distribution. In the next step, the

DOI:10.15774/PPKE.ITK.2018.003

damping constant is set to its real, low value and the oscillating field of the waveguide is applied. The spin waves appear as small (few-percent) perturbations on top of the previously calculated magnetization distribution.

Figure 5.6 shows a snapshot of the magnetization distribution from the simulation. It is a contour plot of the M_x magnetization component (M_y would look similar). An interference pattern is formed, as expected from the theory of the Rowland spectrograph. The results confirm that in the chosen parameter regime, the spin waves behave exactly as expected from the simple picture based on linear waves.

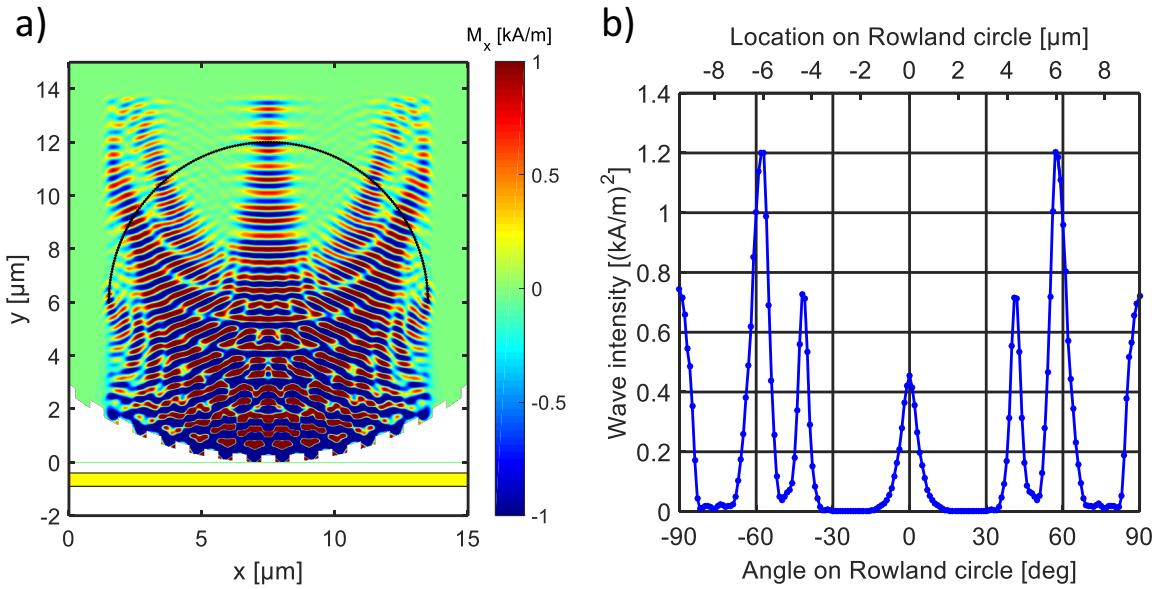

Figure 5.6. Micromagnetic simulation of the spin-wave-based Rowland circle spectrometer. a) The colormap shows a magnetization snapshot of a YIG film, the peaks on the Rowland circle correspond to frequencies $f_1 = 10$ GHz and $f_2 = 10.25$ GHz. The yellow stripe at the bottom is a sketch of the microstrip that is used as a source. b) Spin-wave amplitude along the Rowland circle indicated by black arc in a).

Figure 5.6b shows the amplitude of waves in the simulation on the Rowland circle. The finite width of the peaks is caused by diffraction, which should set the width of peaks to be approximately equal to the wavelength, and this is exactly what is seen in the output intensity distribution of Fig. 5.6. In the simulated device, this allows to resolve only a few (approximately four) peaks – but this is due to the very small simulation domain.

The amplitude of the two frequency components in the microwave signal were set to be equal, but one can see in Fig. 5.6 two different amplitudes corresponding to these frequencies. This is due to the geometry of the grating we used. On this grating, all wave components

DOI:10.15774/PPKE.ITK.2018.003

experience the same periodic shifting in distance, but this distance shift corresponds to different phase shifts depending on the wavelength. Thus the grating is not equally effective at every wavelengths, which results indifferent amplitudes. Spin-wave-generation efficiency of the waveguide also becomes smaller at shorter wavelengths, and the damping can also play a role in large device sizes. In case of the above example, a 250 MHz frequency separation in the input signal translates to a factor of approx. 1.5 change in the spin wave wavelength, which, in turn results in less than a factor of two difference in the intensity of the peaks at read-out. All the effects described above can be taken into account by proper scaling (calibration) after the read-out.

For most practical purposes, one will have to use a device that is few hundred to few thousand times the size of the chosen spin wave wavelength. Direct micromagnetic simulation of structures with such size is not possible, but we expect that scaling up the device does not introduce unexpected effects, and the conclusions we have drawn from the above simulations remain valid.

The curved grating is central to the function of the device and this is the one that requires high-quality, nanoscale fabrication resolution. If the boundary of the grating is different from the ideal, rectangular shape (e.g. all edges are rounded and not sharp), but the structure is periodic to a good approximation then these variations will only change the power distribution between different-order peaks. Non-periodic changes will degrade the spectral resolution. Since the wavelength range is a design parameter, one may choose to use longer-wavelength (dipole-dominated) waves if high-resolution patterning of the magnetic film turns out to be difficult of overly expensive. YIG patterning in notoriously challenging, but is demonstrated for hundred nanometer size scale features [40]. One could also imagine other types of grating structures for generating and manipulating the spin waves [41].

For the device to work as a Rowland spectrograph, spin waves should display linear interference pattern – and this requires proper setting of the excitation amplitude. In order to estimate the excitation range, where linear waves are generated to a good approximation, we analyzed spin wave propagation in various one-dimensional structures, using different excitation amplitudes and a similar antenna geometry to the one described here. The spectral decomposition (Fourier transform) of the time-dependent magnetization was studied at certain points in the simulated structure. We found that the spectral components that arise from nonlinear effects were at least two order of magnitude smaller than the signal up to an excitation current four times what we used in the above simulations. In the presented simulations, the maximum precession angle (at the point of spin wave generation) is around five degrees, and waves remain safely in the linear regime.

All simulations were done at $T = 0$ K, i.e. they do not take into account thermal agitation of the magnetic moments. Thermal fluctuations appear as a wideband noise on top of the spin-wave signal and they superpose to other noise sources, such as the Johnson-Nyquist noise in the electrical components. Preliminary calculations show that the magnetic noise will be negligibly small compared to Johnson-Nyquist noise in the magnetoelectrical interfaces [42].

DOI:10.15774/PPKE.ITK.2018.003

5.6 Magneto-electric interfaces

A practical signal processing device has electrical inputs and outputs – even if signal processing itself is done outside the electrical domain. Conversion of electrical signals into spin-wave signals is the easier part as a relatively simple waveguide geometry may be used. But energetically, this is an inefficient process. In the literature of YIG-based devices, one typically finds that magnetostatic waves appear as a few-hundred ohms per centimeter load to waveguides [43]– this means that for the at most millimeter-sized device proposed here, the magnetic film represents a rather small load to the waveguide. Most microwave energy is dissipated at the load terminating the waveguide and only a few percent of the microwave energy is converted into spin waves. Still, only a few milliwatts of microwave power is required for wavefront generation, which is very small compared to the often several-watts consumption of microwave devices. There are potentially more power efficient and more practical ways for spin wave generation: magneto-elastic effect is a promising, demonstrated technique that may substitute the waveguide-based generation [44]. Spin-orbit torque (Spin Hall Effect) [45], possibly used with a patterned waveguide, could be especially practical for short-wavelength spin wave generation. Spin-orbit torque, with sufficiently anisotropic materials could also make the external field biasing redundant [45]. Spin-torque is an established method for short-wavelength spin wave generation [20], albeit less trivial to use in magnetic insulators such as YIG [46]. Spin-torque oscillator like structures could be driven by AC currents, as required in this application [47].

A more significant challenge, lies in converting the very low-energy spin-wave signals back to the electrical domain. Read-out of spin waves is possible by micron-scale antennas or using the inverse spin Hall effect (iSHE) [48]. In either case, the output signal will be in the few-ten microvolt range [42], but for the antenna-based pickup it will be an AC voltage, while iSHE results in a DC output.

For antenna-based pickup of spin waves, we presented a case study in [42]. The specifications and engineering challenges for the pick-up circuitry are very similar to what one faces in the first stages of a microwave/radio-frequency receiver. For few-micrometer sized antennas, one expects microvolt signal levels. Receiving and amplifying microvolt signal levels at these frequencies requires significant circuitry – both amplifiers and filters that restrict the bandwidth in order to limit resistive noise. Similar pick up circuits were already realized for different purposes [49] and the possibility of using CMOS up to 100 GHz [42] certainly boosts the practicality of such a solution.

Inverse Spin-Hall effect-based readout could be more practical as the resulting DC voltage can be picked up with a slower amplifier circuit and no filtering and mixing is required [48]. Most likely, however, one needs circuit techniques to eliminate DC drifts and if high output date rate is required, resistive noise will limit the dynamic range of the read-out and the dynamic range of the entire spectrum analyzer. Regardless of the chosen method, the output signal is proportional to the area where spin wave intensity has to be detected, and the magnetoelectric conversion will be more challenging for the short wavelength, exchange-dominated regime.

DOI:10.15774/PPKE.ITK.2018.003

It is expected that the power consumption, area and complexity of the output circuitry will dominate the complexity of the entire spectrum analyzer - outputs are the Achilles heel of all spin-wave based devices. Still, the proposed spectrum analyzer performs a rather complex signal processing function with relatively few inputs and outputs, and has smaller overhead than, for example, spin-wave-based logic or computing devices, many of which requires magnetoelectric conversions between gate-level building blocks [50].

5.7 Conclusions and outlook

New nanoscale computing devices often target power-efficient switches that could possibly replace CMOS devices for future circuits and keep Moore's law going [50]. However, it is a tall order to beat CMOS devices in all figures of merit. Sub-threshold CMOS devices could be extremely power efficient albeit slow – but one can trade power for high-speed operation, if needed. In this chapter, we argued that high-speed and low-power special-purpose processing may be an application area where spin waves may significantly outperform electrical-circuit-based solutions. The proposed signal-processing device also exemplifies a non-Boolean computing primitive – a special-purpose computing task, which is not computationally universal, but can be immensely useful in many applications. One may envision similar optically-inspired spin-wave devices, such as lenses and mirrors to perform Fourier transformation and filtering [47], or holographic pattern matching.

Microwave signal processing, up to several hundred gigahertz frequencies could be a real market niche for spin-wave-based processors [10]. Most spin (wave) based device proposals target computing and logic applications, competing with proven CMOS-based approaches. Microwave structures may turn out to be a natural application area for spin waves, and an area where no competing transistor-based solutions exist.

DOI:10.15774/PPKE.ITK.2018.003

Chapter 6

SPIN WAVES IN METAL-INSULATOR MAGNETIC BILAYERS[1]

6.1 Introduction

Spintronic devices (such as spin-torque oscillators (STOs), magnetoresistive structures, etc.) are made from amorphous, metallic ferromagnets (Permalloy, CoFe, etc.) that are conductors and can be deposited and patterned with straightforward technologies. It is also experimentally demonstrated that short-wavelength spin waves can be generated in such ferromagnetic thin films [20], which opens the way for spin-wave based computing devices. Due to the large damping constant of metallic ferromagnets, the typical spin wave decay length is on the order of 2 μm [20], so only very small-scale spin-wave devices can be built [52]. Strong damping also comes with high thermal noise, which degrades signal integrity. Spin-wave based computing blocks must be scalable beyond a few micrometer size, since magneto-electrical interfaces and/or spin-wave amplifiers require a large energy and area footprint.

Unlike metallic ferromagnets, Yttrium Iron Garnet (YIG) is an excellent medium for spin-wave propagation, having one to three orders of magnitude smaller magnetic damping than Permalloy [53]. But YIG is an insulator, and it is challenging to deposit high-quality YIG thin films as well as to pattern YIG on the nanoscale. Spin-waves in YIG are usually excited by RF antennas and it is very difficult to excite short-wavelength, exchange-dominated waves this way. Magnetostatic waves can be straightforwardly excited but they typically have several micrometers or longer wavelength [36], making them impractical for microelectronics applications. In fact, most experimental studies on YIG-based devices deal with long-wavelength magnetostatic waves, and it is often taken for granted that the devices will be scalable all the way down to the regime of exchange waves [7].

It remains a fundamental challenge for spin-wave-based devices that no material is known that would simultaneously allow low-damping propagation of short-wavelength spin waves and electrical generation/manipulation/detection of spin waves in nanoscale magnetic structures. We address this problem proposing a magnetic bi-layer, which is built from permalloy nanostructures grown on top of a low-damping YIG film. In essence, one layer supports spin-wave propagation, while the other layer is used for the electronic interface.

The operation of the proposed structure relies on exchange and dipolar interactions between a continuous YIG film, and patterned Permalloy-based devices and layers on top of this film. Spin waves created in the Permalloy layer can be injected in the YIG film and the local stray field from nanomagnets on top of the YIG film can alter the propagation of the

[1] The results presented in this chapter corresponds largely to [51]

DOI:10.15774/PPKE.ITK.2018.003

spin waves inside the YIG film. The YIG layer need not to be patterned and is used as the low damping propagation medium.

Similar bi-layers were studied for applications in bubble memories [54], and very recently, spin-wave propagation in these bilayers was characterized as well [55], [56]. To our knowledge, no application areas for such bi-layers (apart from the now obsolete bubble memories) were proposed.

In Section 6.2 of this Chapter, we describe a computational model of the coupled Permalloy - YIG system. These micromagnetic simulations show that if an STO free layer is in close proximity of a YIG film, then the dipole and exchange interactions strongly influence the propagation of exchange waves in the film - these results will be presented in Section 6.3. The following Section 6.4 discusses various scenarios for injecting exchange waves in the bilayers. In the concluding section we attempt to evaluate the potential of these device components for information processing.

6.2 Micromagnetic model of the permalloy-yig system

We used the established OOMMF [15] code and studied the behavior of spin waves by postprocessing time-domain results.

For Permalloy, we used values for saturation magnetization $M_s^{Py} = 8.6{\cdot}10^5$ A/m, exchange stiffness $A_{exch}^{Py} = 1.3 \cdot 10^{-11}$ J/m, and damping constant $\alpha^{Py} = 0.008$. For YIG, we used saturation magnetization $M_s^{YIG} = 1.6{\cdot}10^5$ A/m, exchange constant $A_{exch}^{YIG} = 4{\cdot}10^{-12}$ J/m and approximated the damping constant $\alpha^{YIG} = 0.001$ [57]. We assumed K = 0 crystalline anisotropy for both materials[57].

One of the most important parameters of our simulations is the exchange parameter between the YIG and the permalloy layer, which characterizes the strength of the ferromagnetic interaction between the magnetic layers. Neglecting higher-order interaction terms, the ferromagnetic interaction can be described either by a J bilinear exchange constant, or an $A_{\text{interface}}$ interface exchange stiffness. There are surprisingly few experimental works characterizing this interaction. Chun et. al. [58] studied an Fe/YIG system, finding a high $A_{\text{interface}}$, typical of coupled metallic ferromagnetic layers. Youssef et. al. [55] measured a similar system using FMR techniques [59] [60], but the resulting exchange constant is much lower and more similar to values found in exchange-coupled layers.

In our simulations, we used the $J = 1.8 \cdot 10^{-4}$ J/m^2 value[55] as the lower bound for the interaction, and we studied spin-wave behavior for higher interaction strengths as well.

In order to study wave propagation (for the simulations of Section 6.3 and 6.6) we created spin waves in the YIG film by a high-frequency spin torque current. This is an artificial way and serves only the purpose to study wave propagation; we study realizable scenarios in Section 6.4. We also used a relatively coarse numerical grid ($\Delta x = \Delta y = \Delta z = 5$ nm) to avoid exceedingly long simulation times.

To set the magnetization direction in the film and keep it from breaking to domains, we applied a B_{ext} = 0.9 T external magnetic field at 87° out of plane. For the simulation, we define a linearly increasing damping coefficient in a 25 nm region around the edges in order to realize absorbing boundary conditions.

DOI:10.15774/PPKE.ITK.2018.003

6.3 Exchange-wave propagation in a coupled yig-permalloy bilayer

The dispersion relation for exchange-dominated waves is textbook material and for simplified geometries, analytical solutions are available [36]. We numerically determined the $f(k)$ and $H(k)$ functions for our geometry and the results are shown in Figure 6.1. Note that the frequency ranges (few tens GHz) and the wavelengths ($\lambda < 100$ nm) are both highly compatible with potential micro and nanoelectronic applications.

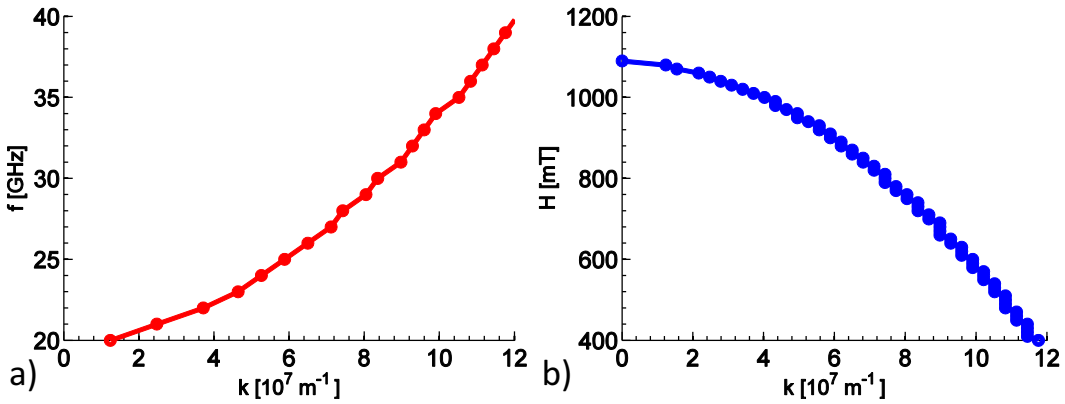

Figure 6.1. Dispersion relation in a 5 nm thick YIG film. a) the frequency - wavenumber relation. b) The external field - wavenumber relation. Wavelengths ($\lambda = 2\pi/k$) and frequencies are ideal for many nano/microelectronic applications.

If a 5 nm thick Permalloy layer is placed on top of a 5 nm YIG film, then the two layers interact via dipole and exchange interactions. For the studied geometry, assuming the lowest estimate for $A_{\text{interface}}$, exchange interaction is dominant. Fig 6.2 shows a pseudocolor plot of the dispersion relation for various $A_{\text{interface}}$ values. The plot was generated by taking the spatial Fourier transformation of the spin-wave amplitude in YIG, so if multiple modes are present, their relative intensity is shown as well.

For small interaction strengths, the dispersion curve shifts to higher frequencies – qualitatively, this is a consequence of the higher effective exchange stiffness that the YIG layer experiences. A low-frequency node appears for higher coupling strengths, which is a propagating exchange wave in Permalloy. We verified this by running simulations for a stand-alone Permalloy layer under the same conditions as Figs. 6.2a-e, and the $f(k)$ curve is almost identical to the low-frequency mode of Figs. 6.2c-e. The Permalloy mode remains weak, even for stronger coupling strengths, and it appears that the damping in the YIG film is not significantly increased by the Permalloy film on top.

At a given excitation frequency, the wavelength shift caused by the Permalloy overlayer can be interpreted in such a way that the Permalloy overlay changes the effective index of

DOI:10.15774/PPKE.ITK.2018.003

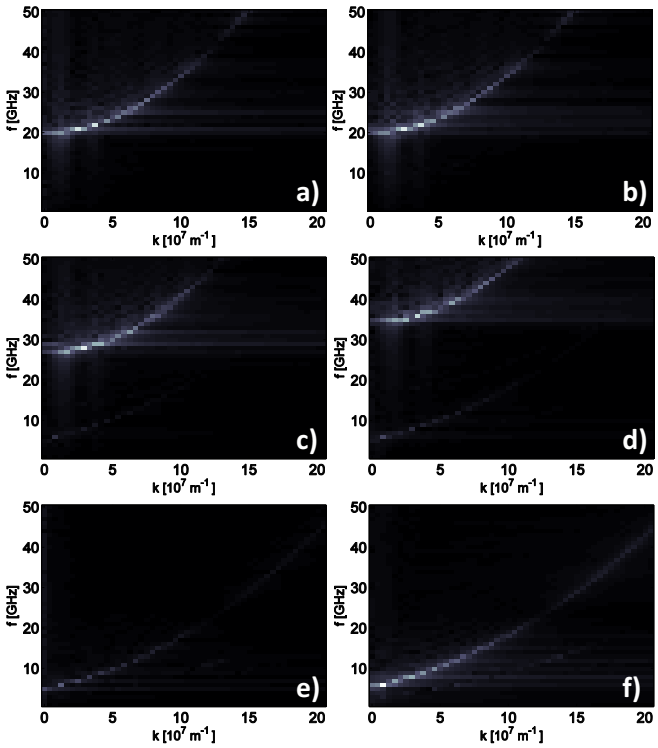

Figure 6.2. Numerically calculated dispersion plots for a YIG-Py bilayer. a) Stand-alone YIG film. b) $A_{\text{interface}} = 0$ J/m c) $A_{\text{interface}} = 0.5 \cdot 10^{-12}$ J/m d) $A_{\text{interface}} = 1 \cdot 10^{-12}$ J/m e) $A_{\text{interface}} = 6 \cdot 10^{-12}$ J/m f) Single Permalloy film. The YIG mode shifts due to the interaction and an additional Permalloy mode appears for stronger couplings.

refraction of the YIG film. In analogy to optical devices, one may potentially design lenses [47], phase shifters, and holograms for on-chip 'YIG optical devices'.

6.4 Spin-wave injection structures

Exchange waves in YIG can be created by very small-size antennas [7] or nanoscale inhomogeneities of a YIG film [61]. This is very challenging, and probably a primary reason behind the lack of studies concerning exchange waves in YIG. In ferromagnetic conductors, propagating exchange waves can be straightforwardly created by spin-torque oscillators [20]. It may be possible to use the exchange coupling mechanism between the YIG layer and the Permalloy to inject short-wavelength spin-waves into YIG. In order to study the feasibility of such a device, we performed simulations on a spin-torque structure, which is exchange-coupled to a YIG layer. A sketch of a highly idealized arrangement is shown in Fig. 6.3a.

Magnetization oscillations are generated in the free layer of the STO, and via a short protrusion, they arrive in the underlying YIG film. The simulations (in Fig 6.3b) show that the spin waves couple into the YIG layer and propagate there.

DOI:10.15774/PPKE.ITK.2018.003

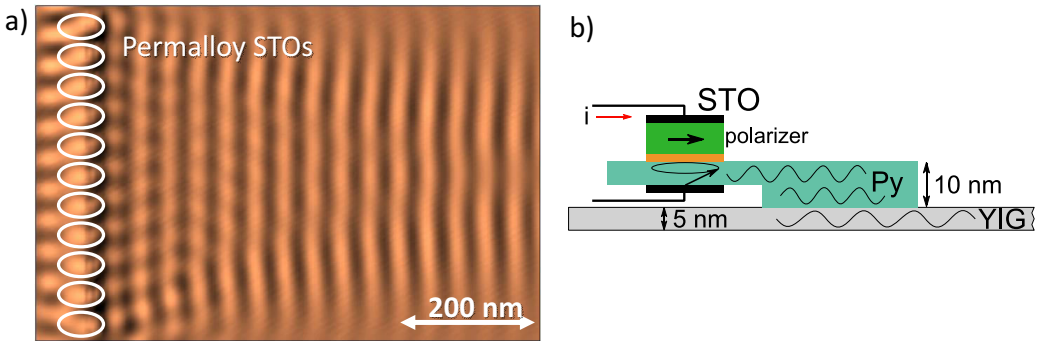

Figure 6.3. a) Waves injected in a YIG film by a line of matching phase STOs. The STOs are phase-locked and generate a coherent waveform, which is coupled into the YIG layer. b) Sketch of the proposed structure for spin wave injection to YIG. The spin waves generated in the Py layer couple into and propagate in the underlying YIG film.

We used an AC current to drive the STO, so the free layer frequency is injection locked to this frequency – this way one can arbitrarily define the phase, frequency and driving current of the STO. We neglected the magnetic field due to the currents in the leads of the STO.

The above-shown models are based on an idealized geometry, but they show that it is in principle possible to inject spin waves from STO-based sources into YIG via coupling between the two films. The size of the spin-wave generating structure ($d < 100$ nm) matches the wavelength of exchange waves, which may allow high-efficiency spin-wave injection into a single propagating mode.

6.5 Magnonic crystals from bilayers

As an example for 'spin-wave optics' devices, we show how a magnonic crystal-like structure can be constructed from the proposed bilayers. Magnonic crystals are mostly made from metallic ferromagnets and are widely studied [62], but their usefulness is severely limited by the high damping of the metallic ferromagnet. Permalloy-YIG bilayer based devices may solve this problem.

The simulation example of Fig. 6.4 shows spin-wave propagation in a YIG film, with Permalloy stripes on top of it. The Permalloy stripes periodically modulate the index of refraction and act akin to a one-dimensional magnonic crystal. Depending on the spacing of the stripes and the wavelength, this periodic potential may reflect or transmit incoming spin waves. The magnonic crystal is defined without patterning the YIG film, circumventing technological challenges and increased damping from rough edges.

6.6 Conclusion

We have shown proof-of-principle simulations for Permalloy-YIG bilayer devices. We argued that this structure unites the benefits of metal-based magnetoelectronic components

DOI:10.15774/PPKE.ITK.2018.003

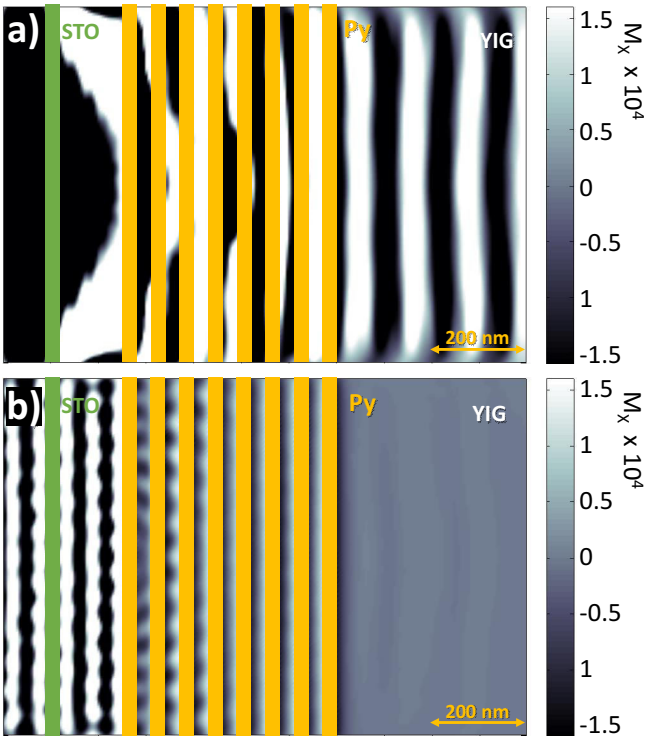

Figure 6.4. One dimension crystal made out of Py on top of YIG film. a) f = 24 GHz b) f = 38 GHz. The position of the 30 nm spaced Permalloy stripes is denoted by the yellow lines. Different frequencies/wavelength may be completely transmitted or reflected by the crystal.

and low-damping YIG films, and can have potential for spin-wave based signal processing devices.

There are a number of ongoing efforts aiming to incorporate YIG (or similar low damping materials) into spintronic devices – spin Hall effect (SHE) is one promising way to do that [57]. Our work shows a complementary approach, which does not require the use of new physics phenomena, rather, it relies on the integration of known spintronic devices with YIG. Balinsky et al. refer to our work and present measurement results on the dipole coupling between YIG and an STO structure in [63].

DOI:10.15774/PPKE.ITK.2018.003

Chapter 7

CONSTRUCTION OF A FERROMAGNETIC RESONANCE MEASUREMENT SETUP BASED ON A TIME DOMAIN REFLECTOMETER

Ferromagnetic resonance measurement of magnetic materials and structures is one of the most important tool for the characterization and extraction of magnetic parameters, most importantly the saturation magnetization and damping coefficient. Although the saturation magnetization can be measured using other common methods, e.g. using vibrating sample magnetometer (VSM), a significant benefit of the FMR measurement is that there is no need for volume estimations, a magnetic sensor calibration is sufficient.

There are two main different types of FMR setups, the conventional FMR, and the Vector Network Analyzer (VNA) based VNA-FMR. In the conventional setup, the measurement is done at only one frequency, using a lock-in technique. The sensitivity can be further increased by the use of a cavity resonator. An FMR curve is obtained by sweeping the applied magnetic field. In the VNA setup, the frequencies are also swept besides the magnetic field, which gives a much more powerful tool for characterization. Using a VNA, a very good signal-to-noise ratio (SNR) is achievable, but careful and precise calibration is required, and it is more costly than the conventional setup.

In principle, a time-domain reflectometry (TDR) measurement can be performed instead of the VNA measurement, the connection between the two methods being a Fourier transform from time domain to frequency domain. However, it is not very common to use TDR in FMR measurements, and the available literature on similar setups is very limited. Pulsed inductive microwave magnetometer (PIMM) [64] is a similar technique in that it uses time-domain excitation and detection of magnetic resonances. The benefits of using a TDR oscilloscope in place of a VNA are that TDR instruments are less expensive than VNAs, and require less precise calibration, while a single measurement gives a wide frequency coverage. However, as we also found, this comes with a rather low SNR and limited frequency resolution.

7.1 Measurement setup

We choose to build a setup based on an old Tektronix CSA 803 oscilloscope with a two-port SD-24 TDR/Sampling head, with 20 GHz typical bandwidth, and 28 ps TDR incident rise time. The bias field was generated by a custom-built four-pole electromagnet (originally built for a different setup), with four removable coils (each of them limited to 3.5 A current or 15 V voltage). Two micromanipulators were attached on the massive poles of the electromagnet. We performed out first measurements on gold coplanar waveguides (CPW) fabricated on a high-resistivity silicone substrate. The waveguides were connected to the TDR ports by

DOI:10.15774/PPKE.ITK.2018.003

two Picoprobe 40A-GSG-150-P (150 µm pitch size) microwave probes with 3.5 mm precision connector cables. A schematic diagram of the system can be seen in Fig. 7.1.

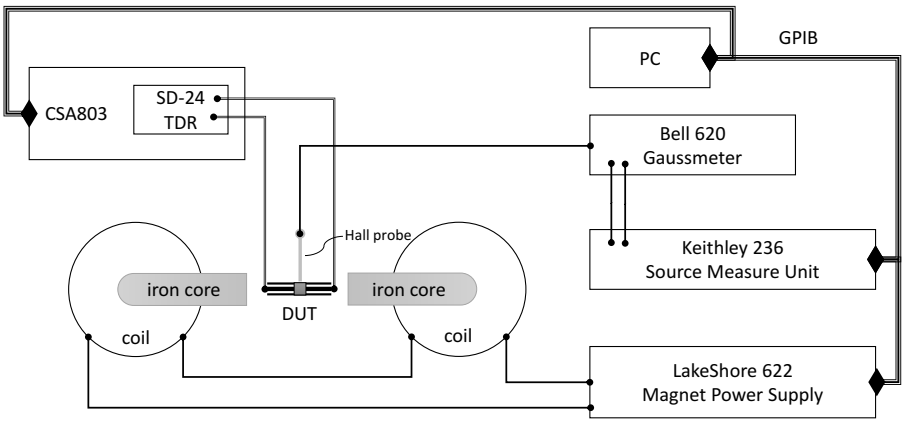

Figure 7.1. Schematic diagram of the FMR measurement setup.

To monitor the magnetic field applied to the sample, an old analog Bell 620 gaussmeter with HTF99 linear Hall probe (30 kG range) were used, connected to a Keithley 236 Source Measure Unit, to digitize the reading. The current for the electromagnet was supplied by a LakeShore Model 622 Magnet Power Supply, with a capability to source up to 125 A current with a maximum voltage of 30 V. Every equipment in this test setup were chosen from the already available instruments in the lab to minimize initial investment costs. To realize automatic control, a PC was connected to the instruments via GPIB port, and a control algorithm was implemented in MATLAB. The algorithm has two main parts, the first is the control of the TDR oscilloscope and data acquisition, while the second is the magnetic field control and stepping, realized by a feedback control loop. The acquired data is saved for subsequent postprocessing. The landing of the microwave probes is possible through a USB microscope camera, mounted on moveable stages. A picture of the complete assembled setup is depicted in Fig. 7.2.

7.2 Test results

To test the developed setup, a thin YIG film on GGG substrate was used, fabricated by Hadrian Aquino via sputtering. The approximately 5 mm wide square-shaped sample was placed with the YIG layer down on a coplanar waveguide. This measurement arrangement is often referred as 'flip-chip' (see Fig. 7.3), and does not require waveguide fabrication on top

DOI:10.15774/PPKE.ITK.2018.003

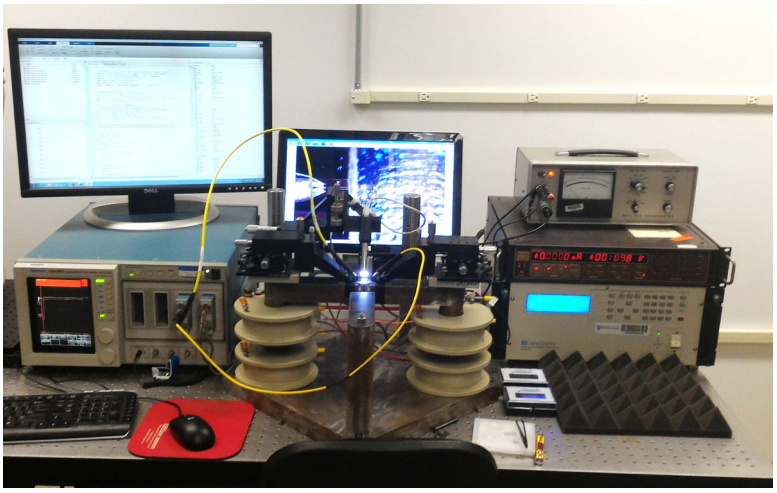

Figure 7.2. The assembled FMR probe station.

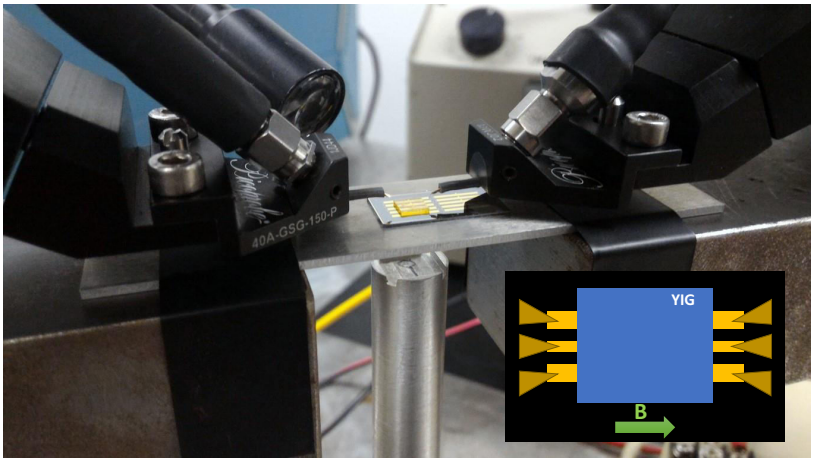

Figure 7.3. YIG sample on the CPW waveguide in the 'flip-chip' configuration. The inset is a sketch of the waveguide with the YIG sample on top and probe tips connected to the waveguide. The arrow indicates the bias field direction.

of the magnetic material. The CPW waveguides were fabricated by Himadri Dey by e-beam lithography on a high resistivity silicone substrate, with gold as the conductor. The nominal width of the signal line was 64 µm, the gap was 13 µm, and the width of the ground lines was 300 µm. The length of the waveguides was 8 mm. The measured characteristic impedance of the waveguide was less than the desired 50 Ω, around 40 Ω, which does introduce some power loss and reflections, but it was not very significant in case of our FMR measurements.

The goal of the FMR measurement is to record the ratio of absorbed energy as a function of magnetic field and frequency. In the constructed setup, the magnetic field was stepped through the desired field values in a controlled way. At every magnetic field step, a TDT

DOI:10.15774/PPKE.ITK.2018.003

(Time Domain Transmittance) measurement was performed, and during the measurement, the magnetic field was kept constant. The TDT measurement was started only after the newly set magnetic field was stabilized within 0.5 G. This was achieved by a closed-loop control mechanism, and the whole process was controlled by a Matlab script on a PC.

The TDT measurement at every magnetic field step consisted of 256 consecutive acquisitions, which were averaged by the Tektronix CSA 803 oscilloscope, and subsequently the data was sent to the PC for postprocessing. The measured TDT signal contained 5120 data points, which is the limit of the oscilloscope's software. The time step for the measurement were chosen to be 2 ps, which means approximately 10 ns time window.

Port 1 of the oscilloscope's sampling head has the built-in step-generator turned on, while Port 2 is sensing the transmitted signal. The recorded TDT signal contains the incident voltage values at Port 2 in function of time. The original step function is degraded after being partially reflected by imperfections in the cable, by non-perfect connections, and also by the effect of the FMR. Since we used inexpensive cables and we did only basic calibrations on the system before the measurement, these effects dominate any changes caused by FMR, and it is impossible to see the effect of FMR with bare eyes (see Fig. 7.4). We need to transform the signal to the Fourier domain to be able to see the effect of FMR at different frequencies. Since we used a unit step function to excite the sample, we need to differentiate the unit response to get the impulse response of the system. We know that the spectrum of an impulse (delta function) is constant, i.e. in theory it is equivalent to probing the system with all the frequencies at the same time (what the VNA does sequentially). By applying Fourier transform on the impulse response, we obtain the system's transfer function in frequency space, which is the same as what a VNA would measure.

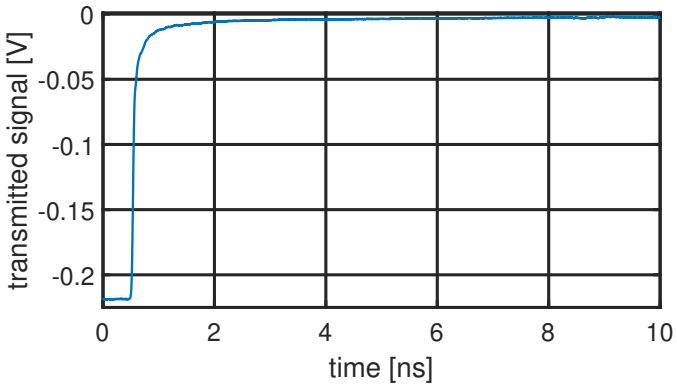

Figure 7.4. Step response measured at Port 2 of the oscilloscope. This signal contains the effect of FMR resonance and also other microwave contributions from the system. The FMR signal is indistinguishable for the naked eye.

DOI:10.15774/PPKE.ITK.2018.003

However, this signal still contains all the effects of the whole system, not only the FMR contribution, which is a very weak signal in comparison. The effects that do not depend on the magnetic field can be separated by the use of a reference measurement, where the magnetic effects are 'turned off'. It is usually true that magnetic effects, other than of the sample, are negligible in the system, since non-magnetic materials are used in the critical components (cables, connectors, probes, etc.). Of course this can not eliminate any time-varying effects, like noise or drift. The most common way to achieve this is applying the magnetic bias field perpendicular to the waveguide instead of parallel to it. This way, the excitation efficiency of the waveguide greatly reduces, since the magnetic field is approximately parallel to the magnetization vector, thus the applied torque on the magnetic moments is very small. Since this requires the ability to apply magnetic field perpendicular to the field used in the measurement (without touching any other component in the setup), an extra component would be required in the setup. We did not have this ability in our setup, so we used a modified version of this method. In unstructured magnetic samples, we only expect one resonance frequency peak at a certain magnetic bias field, and the absorbed energy at frequencies far from the resonance frequency is negligible. Thus, if we apply a field outside the measurement field rage (e.g. the highest field that the system can achieve), the recorded transmittance spectrum can be used as a reference for the other measurements as long as the bias field is not very close to the reference field. We further modified this method, and instead of a separate reference measurement, we averaged out all the spectra measured at different bias fields. This way, the differences between the curves at different bias fields (i.e. the resonance peaks) will diminish in the average (less than one percent if more than a hundred measurements were taken), so it can be used as a reference. The main advantage of this method is that it also offers noise reduction, as opposed to the previous method, where the noise in the reference measurement is added to all the other curves (e.g. a noise peak in the reference will appear in the final spectrum at every bias field).

The measured FMR curve is depicted in Fig. 7.5, after subtraction of the reference measurement, and removing the effect of drift. The FMR resonance curve can be seen clearly, it stands out from the noise.

The most important limitations of the TDR-FMR technique seem to be the limited SNR and the limited frequency resolution. Note, that the frequency resolution df depends solely on the acquisition time T, $df = 1/T$. The acquisition time was chosen to be 10 ns, which has physical limits, most importantly the length of the cable, since a slight mismatch and imperfect connections will result in reflections back and forth in the cable. The estimated delay of the cables that were used was 3.5 ns, so 10 ns is less than the time it takes for the pulse to be reflected back to the port. The rather low SNR is caused by the limited sensitivity of the oscilloscope, since in case of a step function, the energy is localized around the step, so the signal is very weak after a few nanoseconds. For this reason we found that increasing the time window beyond 10 ns did not improve the SNR of the signal any further.

We fitted Eq. 2.6 on the data (Kittel fit) using the method described in [30]. Additionally, because the fit was not perfect at first, we introduced a field offset B_{offset} and a field scale parameter b_{scale} to represent the possible calibration errors of the gaussmeter.

DOI:10.15774/PPKE.ITK.2018.003

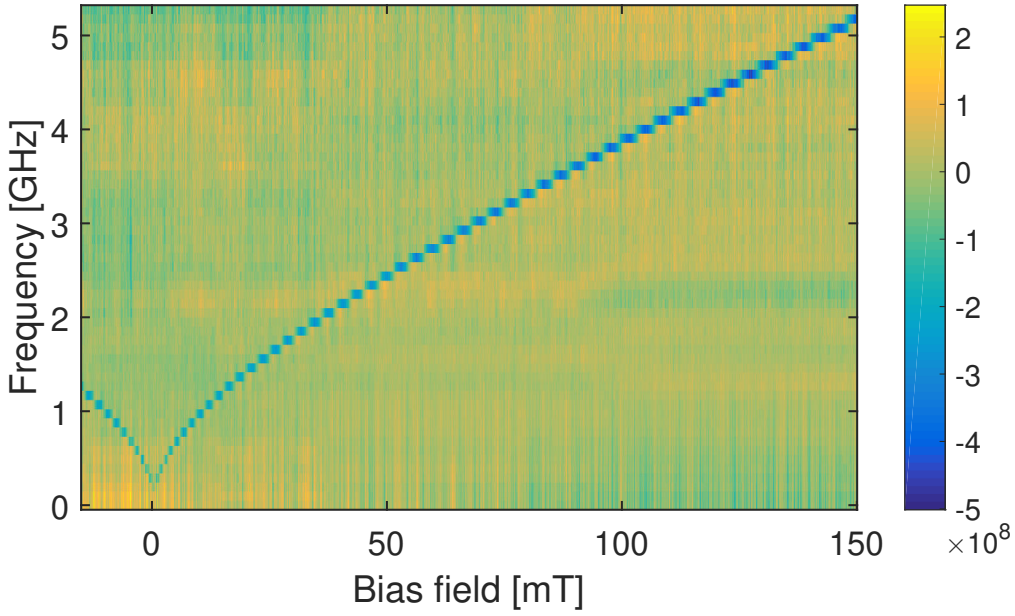

Figure 7.5. Ferromagnetic resonance frequency absorption of a YIG sample measured by the designed TDR-FMR setup.

The fitted curves can be seen in Fig. 7.6, and the fit gave $M_s = 102.5$ kA/m for saturation magnetization, $\gamma = 27.96$ MHz/mT for gyromagnetic ratio, $B_{offset} = 0.94$ mT for bias-field offset error, and $b_{scale} = 0.874$ field-scale error. The saturation magnetization value is lower than the typical value for YIG (around $M_s^{YIG} = 140$ kA/m in [30]), but since the YIG fabrication process has not been optimized yet, it is a reasonable value. The gyromagnetic ratio γ is very close to typical literature values, which is reassuring, since this parameter should not change much among samples. The field offset error is relatively small, less than 1 mT is a very reasonable calibration error, but the scale error is surprisingly large, the fitted bias field values are more than ten percent less, than the measured ones. This could be checked by a better gaussmeter in case of future use of this setup.

We used both derivative-of-Lorentzian, and derivative-of-Gaussian fitting on the FMR peaks, performed on the derivative of the data, using the following function for Lorentzian fit:

$$L'(H) = A\frac{(H - H_{FMR})\,\Delta H_{FMR}}{\left(4\,(H - H_{FMR})^2 + \Delta H_{FMR}^2\right)^2}, \tag{7.1}$$

and for Gaussian fit:

$$G'(H) = A\frac{(H - H_{FMR})}{\sqrt{2\pi}\left(\frac{\Delta H_{FMR}}{2\sqrt{2\ln 2}}\right)^3} e^{\frac{-(H-H_{FMR})^2}{2\left(\frac{\Delta H_{FMR}}{2\sqrt{2\ln 2}}\right)^2}}, \tag{7.2}$$

where H_{FMR} denotes the center, and ΔH_{FMR} denotes the full width at half maximum (FWHM) of the resonance peaks, and A is a scaling factor. An example for both types of fit can be seen in the inset in Fig. 7.6. Note that Gaussian fit matches better the data, which means that the linewidth broadnening caused primarily by inhomogeneity, rather than damping [65].

DOI:10.15774/PPKE.ITK.2018.003

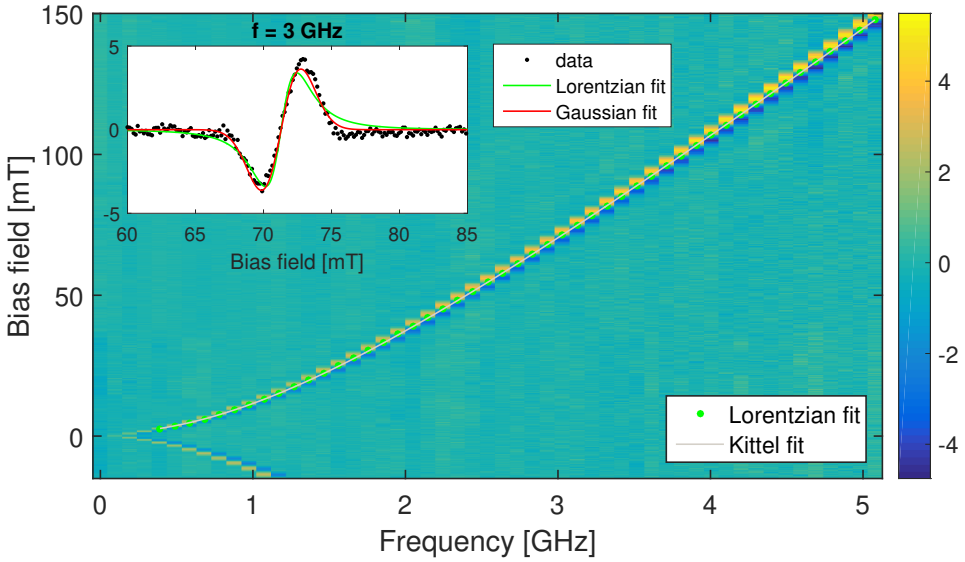

Figure 7.6. Kittel fit on the measured FMR data. The colormap shows the derivative of the FMR absorption data. The inset shows the Lorentzian and Gaussian fit at 3 GHz as an example.

To estimate the damping of the sample, we examined the linewidth of the FMR peaks. The damping can be calculated from the linewidths using the following formula[30]:

$$\Delta H_{FMR} = \Delta H_0 + \frac{2\alpha}{\sqrt{3}|\gamma|} f, \tag{7.3}$$

where ΔH_0 denotes film inhomogeneity line broadening. Note, that the value of damping is not directly proportional to the linewidth, instead it is proportional to the change in linewidth in function of the frequency. The damping value was estimated by a linear fit to Eq. 7.3, the fit is plotted in Fig. 7.7. The fitting yields a rather high damping value, $\alpha_L = 0.0182$ in case of Lorentzian fit, or $\alpha_G = 0.0155$ in case of Gaussian fit, and also large inhomogeneity broadening $\Delta H_{0L} = 1.53$ mT and $\Delta H_{0G} = 1.34$ mT. Since the saturation magnetization value was not close to the expected YIG value, these poor linewidth values were not unexpected.

7.3 Conclusion

We developed a home-made FMR setup and we used time domain reflectometry to measure ferromagnetic resonance in magnetic films. In comparison to the VNA-FMR, this method offers significantly lower costs and requires less precise calibration. We found that our TDR-FMR setup has more flexibility than conventional FMR, which only offers single frequency FMR, however, the drawback is the much lower SNR and still lower frequency resolution compared to VNA-FMR. We conclude that at a very moderate cost, even if one uses old components, it is still possible to perform useful FMR characterization, with some limitations which mainly arise from the low sensitivity of the method, and the medium frequency resolution.

DOI:10.15774/PPKE.ITK.2018.003

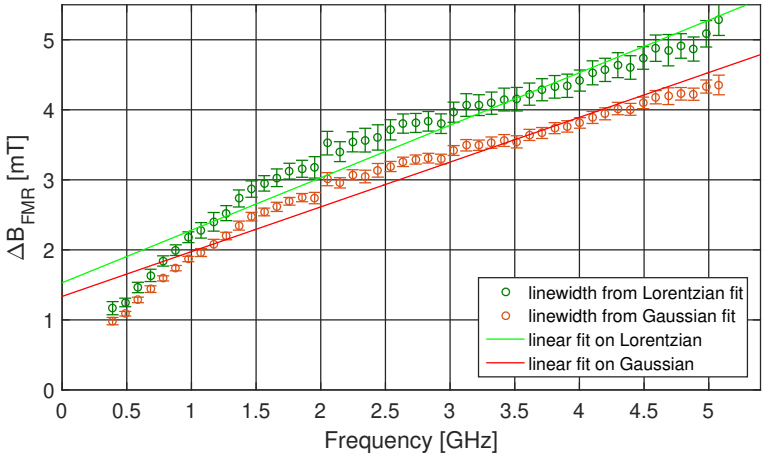

Figure 7.7. Linear fit on FMR linewidth from Lorentzian fit and Gaussian fit. The damping is proportional to the slope of the fitted lines. The errorbars denote 95% confidence bounds.

DOI:10.15774/PPKE.ITK.2018.003

Chapter 8

SUMMARY

In this dissertation, we proposed a new way of computing and signal processing with spin waves. We showed that optical computing principles work well with spin waves as well, and many of the already established concepts can be used to construct spin-wave-based computing devices. This approach is different from previous works in that it uses spin-wave interference patterns to realize complex computing tasks, such as linear transformations, filtering, and signal decomposition. Most of the devices presented in the literature so far applied spin waves as a new signal carrier to realize binary operations. Our approach minimizes the magnetic-electric conversion overhead by performing the function of several gates in a single operation.

Spin waves has many advantages compared to electromagnetic waves in computing applications. Most of today's communication channels and the operation frequency of computing devices fall in the several GHz frequency range. Spin waves have wavelengths in the nanometer–micrometer range at these frequencies, which enables very compact designs, without the need of transferring signals to higher frequency regimes. This means that at microwave frequencies spin waves enable creation of interference patterns at the scale of optical wavelengths. We believe, that this is a very good match for many applications.

Future challenges of spin-wave computing devices include efficient electric-magnetic conversion methods, the integration of low-damping magnetic material in the CMOS fabrication process, and development of efficient high frequency support circuitry for spin-wave circuits. We believe that current technologies are sufficient for the demonstration of some of the devices presented in this work, but still there are several issues to be solved for this technology to be competitive.

8.1 Theses of this dissertation

Here we summarize the original contributions of the author of this dissertation, in a list of theses.

Thesis I. – I have shown that in principle, basic optical building blocks can be constructed for spin waves. I performed micromagnetic simulations to verify the concepts and demonstrate the operation of these devices.

Thesis II. – I proposed the use of a spin-wave lens (or mirror) to perform Fourier transform via spin-wave interference. I used micromagnetic simulations to verify the operation principle of the device for multiple lens designs.

DOI:10.15774/PPKE.ITK.2018.003

Thesis III. – I proposed a new microwave spectrometer based on spin-wave interference. The design is similar to the Rowland spectrograph used in x-ray spectrography, but designed for spin waves. I used micromagnetic simulations to verify the operation of the device.

Thesis IV. – I used micromagnetic simulations to investigate the interaction between YIG and Permalloy films. Based on our findings, we proposed a new way of spin-wave excitation in insulating films and using spin-torue oscillators.

Thesis V. – I designed and constructed a ferromagnetic resonance measurement setup based on a time domain reflectometer. I performed measurements of saturation magnetization and damping coefficient of YIG films.

Thesis VI. – I proposed a threshold gate design for nanomagnetic logic. Novel features of the design include the use of domain-wall conductors for signal propagation, and the use of threshold gates instead of the traditional majority-gate-based designs. I performed micromagnetic simulations to verify the operation of the device.

DOI:10.15774/PPKE.ITK.2018.003

Appendix A

SPIN-WAVE MEASUREMENTS

In this chapter we present our preliminary designs and measurement results for spin-wave generation. Our future goal is to demonstrate the basic concepts of spin-wave interference based devices, and the first step towards performing these measurements is the ability to generate and measure spin waves. Although the work is still incomplete at this point, we think our approach and preliminary results are still of interest and useful for those who might attempt a similar measurement. We designed a spin-wave antenna for efficient generation of short-wavelength spin-waves, that are necessary for compact and low-power spin-wave-based computing devices. The samples described in this chapter were fabricated by Himadri Dey (Notre Dame), and BLS measurements were performed by the group of Professor Giovanni Carlotti (University of Perugia, Italy).

A.1 Short-wavelength spin-wave generation

One of the most critical part of spin-wave-based computing devices is the realization of the spin-wave excitation. An efficient and reliable spin-wave source is crucial to achieve low power consumption. There are a number of proposed techniques to convert electrical signals to the magnetic domain, and among them are nano-antennas that utilize the magnetic field of the electric current, spin-torque oscillators that are based on the spin-transfer torque, spin-hall effect based devices, and electric-field-driven magnetoelectric cells. While interest in the latter three techniques is growing, and experimental demonstrations exist, we found that in some applications a waveguide antenna can perform comparably. We investigated the use of waveguides for spin-wave generation, which does not require exotic materials, challenging fabrication steps, and the physical background is well understood. One of the main limitation of waveguide antennas for spin-wave generation is that waveguides generate spin waves efficiently with wavelengths comparable to the waveguide size. The down scaling of waveguides is limited by ohmic losses, and in our region of interest (below a micron) the lossless waveguide approximation is no longer valid. While the coplanar waveguide (CPW) is the most popular choice in the literature for spin-wave experiments, without exception all of these measurements are done on spin waves with at least several microns of wavelength, which is not very practical in most of the proposed spin-wave-based designs. We investigated the limitations of down scaling of the waveguides and performed test measurements on more compact waveguide designs.

We investigated two different waveguide types, namely the microstrip line (MS) and the coplanar stripline (CPS). These are probably the two simplest waveguide structures consisting of one wire for the signal and another (possibly more spread-out) conductor for the

DOI:10.15774/PPKE.ITK.2018.003

ground. At first, we chose to fabricate a microstrip waveguide, since the field is well confined between the signal and the ground conductors, where the magnetic layer can be placed. However, this attempt was challenging in the fabrication and measurement point of view. BLS measurements of the generated spin waves gave inconsistent results, and further investigations suggested that the magnetic film quality was degraded by the gold ground plane fabricated underneath. This uneven medium probably resulted in scattering of spin waves in the magnetic film. The other important issue of this design was the capacitive effect of the contact pads. Because of the close proximity of the signal and ground planes, the contact pads acted as a huge capacitance at the end of the probes and effectively shorted out the waveguide, allowing only a small fraction of the signal to enter the antenna part.

To avoid the issues that resulted from the gold layer under the magnetic film, we switched to a coplanar design on top of the magnetic layer (this approach is probably a much better fit to be used on top of YIG and similar magnetic garnets which require a special substrate to grow high quality single-crystal layers). The simplest coplanar structure is probably a coplanar stripline, which consists of two conductors separated by a lateral gap. The coplanar stripline is narrower than a coplanar waveguide, and also it is 'open' in one side, i.e. the signal line is not surrounded by wide ground lines on both sides.

A.2 Design of a coplanar-stripline antenna

There are two very important aspects of the antenna design, one is to maximize the power delivered to the antenna part of the waveguide, and the second is to maximize the efficiency of the spin-wave generation. The first goal can be achieved by careful design to minimize mismatches and reflections along the waveguide, and by minimizing ohmic losses, that are very significant in case of sub-micron thick wires. For the second goal, we performed simulations to find the dependence of the generation efficiency on the waveguide geometry. We found that the width of the waveguide is closely related to the efficiency, and for best results the waveguide should be as narrower than the wavelength and also as close as possible to the film. This presents a compromise between the two design goals, as the width and thickness of the waveguide decreases, ohmic losses increase.

To design the waveguide and estimate the magnetic field of the antenna, we used a numerical calculation using Ampere's law and assuming homogenous current in the waveguide.

The overall geometry of the waveguide structure (Fig. A.1) was given by the BLS measurement setup constraints. A 50 Ω GSG probe was used with a 150 μm pitch, and the waveguide had to make a 90° turn, thus we had to include a tapered 90° bend in the waveguide. The end of the line was shorted, this means that the current is always maximal at the end of the line, and it decreases slowly moving further from the short. This variation should be negligible in the measurements, since the scale of the spin waves is at least three orders of magnitude smaller than of the electromagnetic waves in the waveguide. We created multiple designs with different antenna dimensions to be able to compare the measurement results.

The characteristic impedance was designed to be close to 50Ω, although due to ohmic losses the characteristic impedance of the antenna has a considerable complex component. We used Permalloy and CoFe for the magnetic film material, and gold for the waveguide con-

DOI:10.15774/PPKE.ITK.2018.003

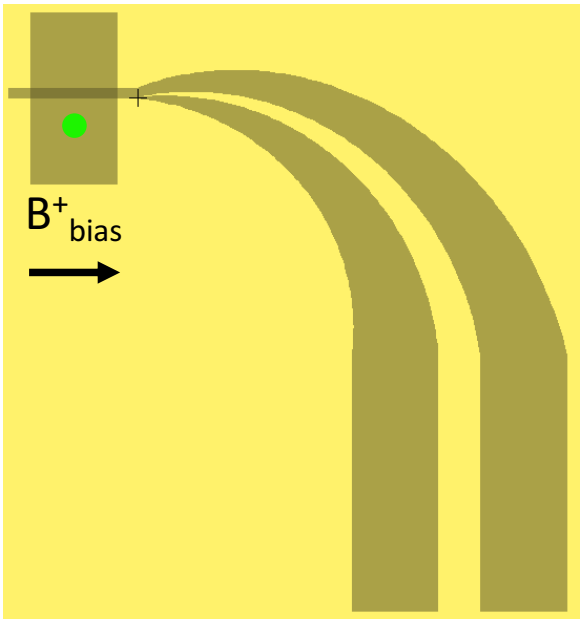

Figure A.1. Layout of the designed antenna including the contact pads and the tapered bend. The green spot shows the side of the waveguide where BLS measurements are performed (next to the signal line). The arrow denotes the 'positive' direction of the bias magnetic field, as we define it.

ductor with SiO_2 as insulator between them. In the long term, it would be interesting to try magnetic materials with lower damping (such as YIG) and better conductors to minimize losses.

Two types of simulations were performed to aid the design and model the generation of spin waves: an electromagnetic simulation using HFSS to optimize the microwave characteristics of the waveguide, and micromagnetic simulations using OOMMF to determine the spin-wave dispersion curve and the generation efficiency.

Fig. A.2 shows the calculated dispersion curves in a 20 nm thich CoFe film with $M_s = 1400$ kA/m, $A = 30 \times 10^{-12}$ J/m and damping $\alpha = 0.008$, under various in-plane bias fields. Simulation results are also included at $B = 20$ mT bias, with good agreement with the calculated curve. The plotted wavevectors are the components perpendicular to the field direction (and in our case also to the waveguide). The wavelength range of interest falls between 1-2 μm. Smaller wavelengths are difficult to measure, while longer wavelengths are less interesting, because only few wavelengths fit in the decay length.

The magnetic field profiles used in micromagnetic simulations were calculated by a simplified model based on Ampere's law, with the assumption of uniform current distribution. This simple and fast method allowed us to test the effect of the antenna parameters on the generation efficiency without unreasonably long electromagnetic simulations. We compared these field profiles to the HFSS results to verify the basic agreement of the two methods, and we found that the structure and the shape of the field is similar in the two methods. The calculated field profiles are shown in Fig. A.3 in case of two antenna designs, one is with

DOI:10.15774/PPKE.ITK.2018.003

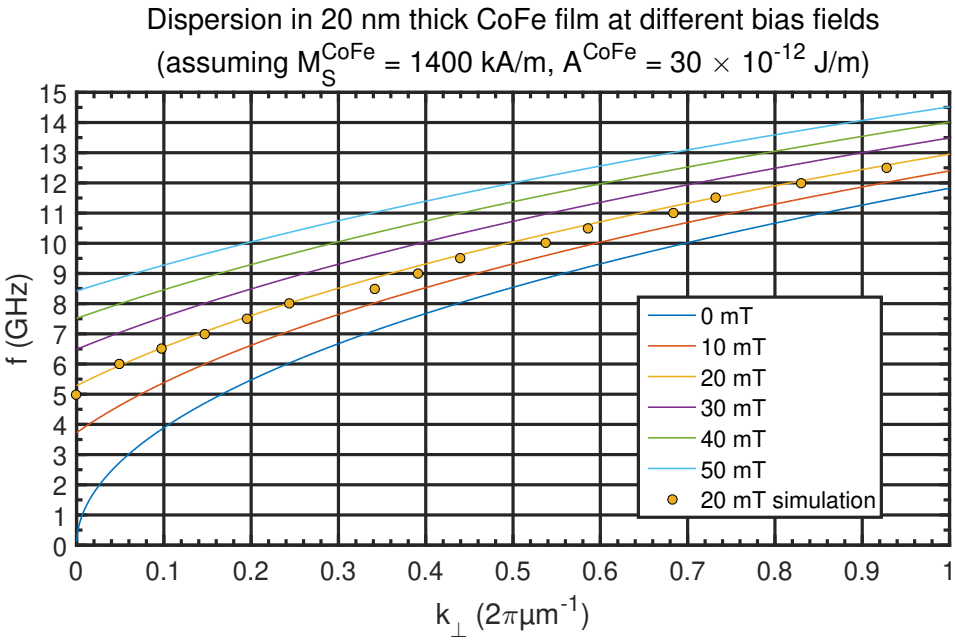

Figure A.2. Calculated and simulated dispersion curves in an in-plane magnetized, 20 nm thick CoFe film. The wave propagation is perpendicular to the field direction. The simulated points are in good agreement with the calculated curves, the deviation is caused by the numerical error in the Fourier transform due to the finite length of the simulated film.

equal signal and ground width (symmetric), and the other with ten times wider ground lines than signal lines (asymmetric). The symmetric line has a narrower field profile overall, while the asymmetric line has more concentrated field profile with a wide low amplitude 'tail'. The asymmetric design has also lower losses because the ground line has lower resistance. We fabricated both designs to compare their efficiency in the generation of spin waves.

The calculated field profiles were used in micromagnetic simulations to excite spin waves in a magnetic film with a one-dimensional discretization. Similar simulations were performed in a range of excitation frequencies between 1-15 GHz, assuming the same excitation current. The resulting excitation profiles can be seen in Fig. A.4 and Fig. A.5.

It can be observed that generally, the optimum frequency of the narrower waveguides is higher than of the wider waveguides. These optimum frequencies correspond to wavelengths approximately half of the overall width of the waveguides. On the log scale plot of the same curve, we can observe several cancellation peaks, where the excitation amplitude substantially decreases around some frequencies. These cancellations are caused by destructive interference among waves that originate from two edges in the waveguide. We labeled the peaks with the corresponding wavelength, and it can easily be seen, that all of them (or their integer multiples) correspond to distances between edges in the waveguide. In case of the asymmetrical designs, the peaks are less distinct since the current density in the signal and ground lines are different, the destructive interference can only be partial.

DOI:10.15774/PPKE.ITK.2018.003

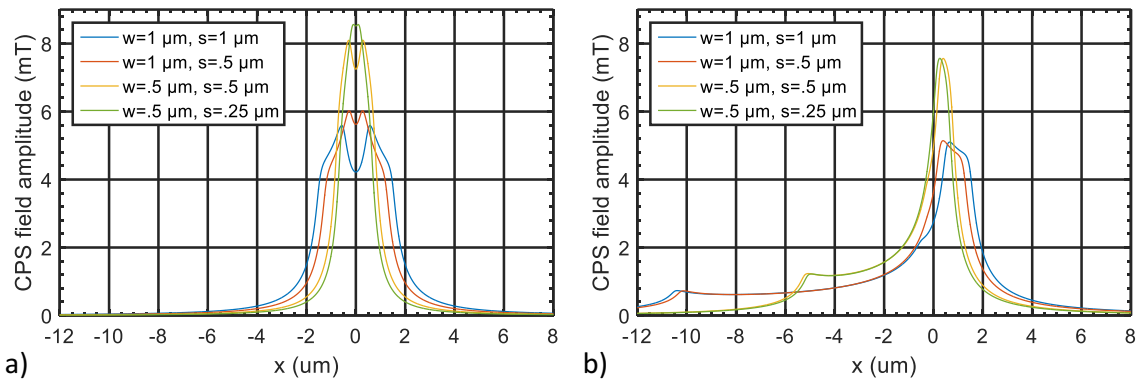

Figure A.3. Magnetic field of the designed CPS waveguides calculated by Ampere's law (w denotes the signal line width, and s the separation distance of ground and signal lines). a) Symmetric waveguides (the width of the ground line equals the width of the signal line). b) Asymmetric waveguides (the width of the ground line is 10 times the width of the signal line).

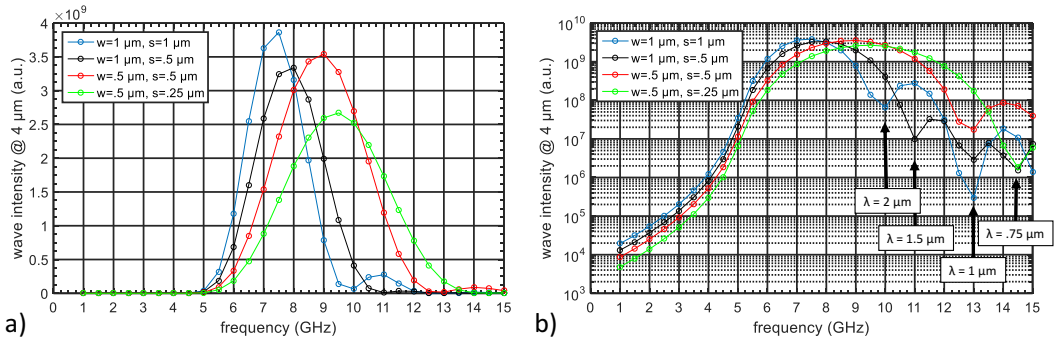

Figure A.4. Frequency dependence of the generated wave intensity in case of the four symmetric waveguide geometries, assuming 10 mA current amplitude.

Overall, we can see that for efficient small-wavelength generation, waveguide sizes below the wavelength should be used. However, this has many difficulties in case of sub-micron wavelengths. Moreover, the antenna has to be carefully designed for the desired frequency band, while wider band operation may need more sophisticated antenna design.

A.3 Brillouin light scattering spectroscopy results

To verify the calculated dispersion curves, phase-resolved Brillouin light spectroscopy (BLS) measurements were performed. BLS relies on the inelastic scattering of photons by spin waves in the magnetic medium [66]. The effect is very small and it is usually detected by a tandem Fabry-Perot interferometer. In microfocused BLS, the laser spot can be focused to a submicron size area, which makes local measurements of spin waves possible. Phase sen-

DOI:10.15774/PPKE.ITK.2018.003

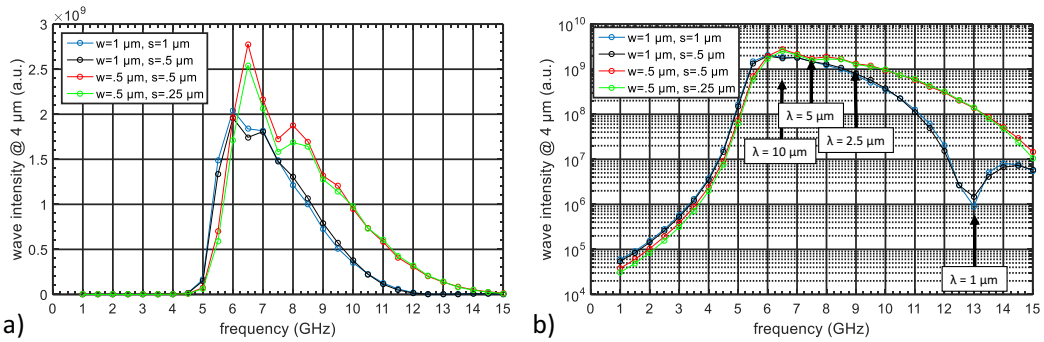

Figure A.5. Frequency dependence of the generated wave intensity in case of the four asymmetric waveguide geometries, assuming 10 mA current amplitude.

sitivity is achieved by modulating the phase of the incident BLS laser beam by the microwave reference signal, using an electro-optical modulator [67]. The modulation amplitude is set to be small, so that it is comparable to the BLS signal. By interfering the reference signal and the BLS signal, a phase dependent amplitude can be obtained. As the spin waves are generated by the same microwave signal as the one used for modulating the laser, the two signals are coherent.

Here, we present preliminary measurement data performed by the group of prof. Giovanni Carlotti (University of Perugia, Italy). Fig. A.6 shows the result of a frequency sweep with the BLS setup at 4 μm distance from the asymmetric waveguides. The graphs can be compared to Fig. A.5, but an important difference is that the measured data contains data about the microwave properties of the waveguides, including losses and mismatches. The dependence is similar to the simulated results, and the cutoff frequency around 5 GHz also matches the simulated curve, except in case of design B, where the cutoff is lower. It is hard to see the high frequency parts of the curves because of the rather high noise, but it can be seen, that the narrowest waveguides perform better at higher frequencies, while the wider waveguides are better at lower frequencies.

Phase-resolved measurements were performed on the four asymmetric waveguide designs, the results can be seen on Fig. A.7. The measurements were performed at 9.7 GHz, except in case of design 'A', where measurements were done at 10 GHz. The wavelengths in case of the 9.7 GHz measurements are close to the value expected from simulations, which was approximately 2.2 μm. The wavelength of the 10 GHz signal is approximately 2 μm, close to the simulated value that can be seen in Fig. A.2. The amplitudes of the spin waves that were generated by narrower waveguides are better, as expected, but again, in the measurements the microwave properties of the waveguide are also included, which result in different excitation power levels.

DOI:10.15774/PPKE.ITK.2018.003

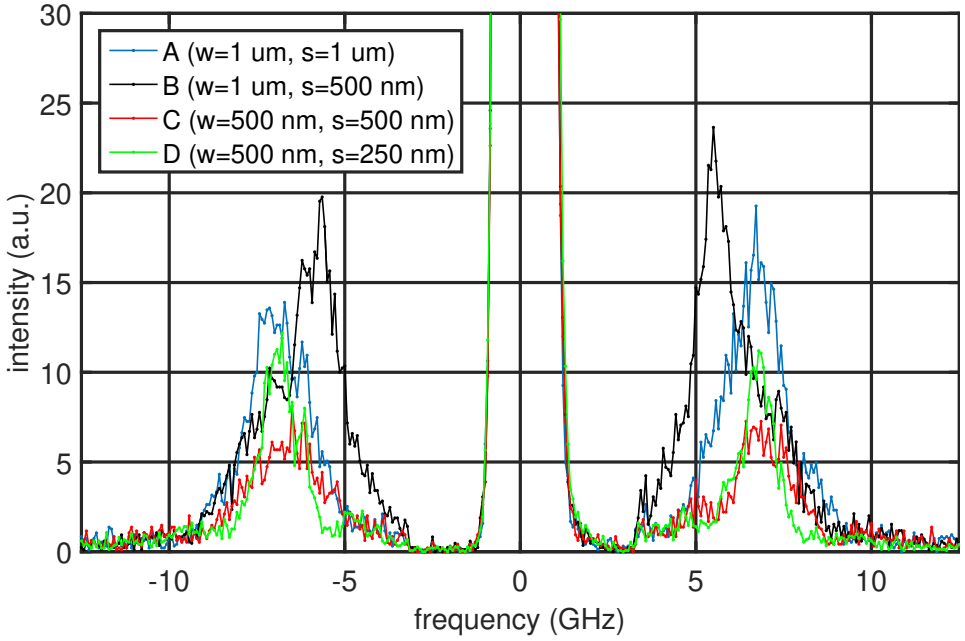

Figure A.6. Measured frequency dependence of the spin-wave intensity at 4 μm distance from the waveguide in case of the four asymmetric waveguide geometries.

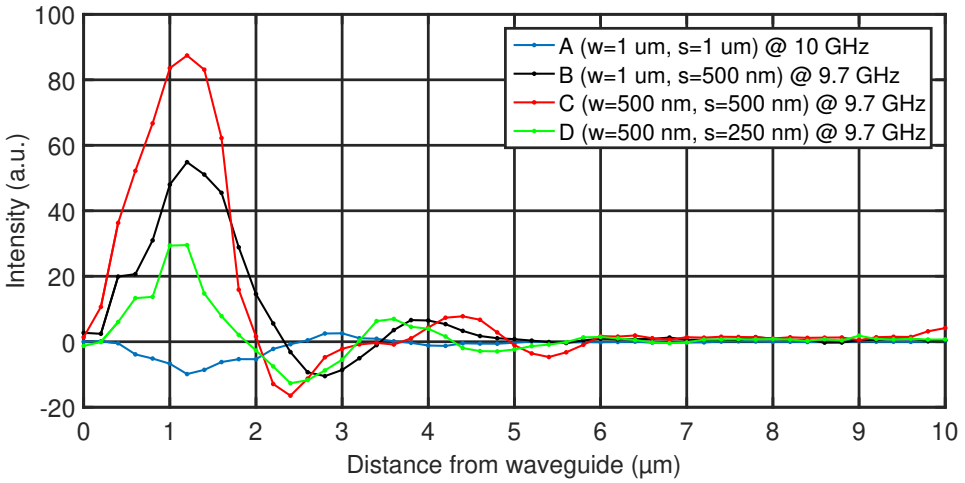

Figure A.7. Phase of spin waves that propagate from the waveguide. The curves are obtained by measuring the interference of the reference signal and the BLS signal. The edge of the waveguides is approximately at 1 μm.

A.4 Conclusion

We designed CPS antennas for short-wavelength spin-wave generation. Our simulations suggest, that generation of spin waves with sub-micron wavelength is possible with waveguides that are wider than the wavelength. However for best efficiency the antenna width

DOI:10.15774/PPKE.ITK.2018.003

should be approximately half of the generated spin-wave wavelength. We found that the current that can be injected into a sub-micron-width antenna, puts strong limitations on the achievable spin-wave amplitudes.

We performed phase-resolved BLS measurements on the generated spin-waves, and we found clear spin-wave propagation. However, the damping in CoFe allowed only a few micron propagation length, thus the signal was fairly small. Future measurements are planned with lower damping materials, that allow longer attenuation lengths. Thus, by manipulating spin waves, simple interference patterns may be tested.

DOI:10.15774/PPKE.ITK.2018.003

Appendix B

NANOMAGNETIC LOGIC THRESHOLD GATE[1]

In almost all NML designs so far, logic functions are constructed from binary gates. Almost all NML circuits (such as the Full Adder of [69]) are designed by simply substituting magnetic AND/OR gates into known gate-level designs. However, more functionality can be realized on the same footprint by actually using the full functionality of majority gates, or further enhancing gate functionality by using threshold gates. Threshold logic gates (TLGs) [70] are well known in the circuit design literature. A TLG-based circuit typically requires 2-3 times fewer number of gates for the same function than a standard AND/OR based design [71]. While synthesis methods for TLG-based circuits are not as established as for circuits comprised of "standard" (AND/OR etc.) logic gates, a large number of designs do exist [72].

In traditional NML, the logic wires and the gates are built from magnetic dots, that are coupled by dipole field. In this chapter, we will show that it is possible to create magnetic logic in a similar way to the dot based NML, but using magnetic stripes (also referred as domain wall conductors (DWCs)). The switching mechanism of a magnetic dot is the same as of a magnetic wire, except the propagation time of the DW in dots is very short.

B.1 Threshold logic gate

In circuit design, a threshold gate is most often defined as an n-input, single-output logic gate, realizing the function

$$\begin{aligned} F^T(x_1 \dots x_n) &= 1 \text{ if } \sum_{i=1}^{n} w_i x_i \geq T \\ F^T(x_1 \dots x_n) &= 0 \text{ if } \sum_{i=1}^{n} w_i x_i < T \end{aligned} \tag{B.1}$$

i.e. the output of the gate assumes a logic '1' state if the weighted sum of its n inputs exceeds a T threshold, otherwise it is 0. The gate inputs and outputs are represented by the $x_i \in \{0,1\}$ logic set.

In this chapter we employ a different form of this definition, which is more suitable to the design of magnetically implemented gates. The logic set $x_i \in \{-1,1\}$ is used instead of the common $\{0,1\}$; and we assume a $T = 0$ threshold:

$$\begin{aligned} F(x_1 \dots x_n) &= 1 \text{ if } \sum_{i=1}^{n} w_i x_i \geq 0 \\ F(x_1 \dots x_n) &= -1 \text{ if } \sum_{i=1}^{n} w_i x_i < 0. \end{aligned} \tag{B.2}$$

[1] The results presented in this chapter corresponds largely to [68]

DOI:10.15774/PPKE.ITK.2018.003

The zero threshold in the definition does not restrict the gate functionality – it is always possible to introduce constant (fixed) x_i^{fix} inputs, which can be moved to the right-hand side of Eq. B.2 and act as a $T = -\sum x_i^{fix} w_i^{fix}$ threshold value.

Fig. B.1 shows the layout of a 4-input TG [73], based on DWCs. The output wire has a specified nucleation area, set by focused ion-beam irradiation (FIB). The external clocking field is set to be near to the switching field of the output wire, and the net field of the input wires in the nucleation area will help or inhibit the nucleation of the DW.

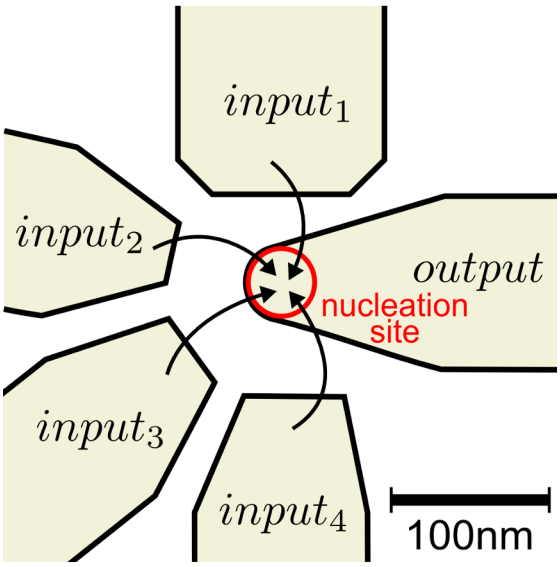

Figure B.1. Layout of a 4-input TLG based on magnetic DWCs.

Per Fig. B.1, we determine the magnetic stray field originating from the four input fingers at the position of the nucleation center:

$$B_z^{cpl} = C_1 m_1 + C_2 m_2 + C_3 m_3 + C_4 m_3, \tag{B.3}$$

where $m_1 \dots m_4$ are the normalized perpendicular (z) component of the magnetization ($m_i = \mathrm{sgn}(M_z^{(i)})$) of the fingers and clearly $m_i \in \{-1, 1\}$. The actual value of the C_i constants should be determined by magnetostatic calculations, and they depend on the shape of the input magnets and on their distance from the nucleation center. Nevertheless, the net stray field will always be a linear superposition of the field of the input magnets in the form of Eq. B.3. If the magnets are in the same plane, then their coupling is antiferromagnetic, i.e. $C_i < 0$.

Assuming fixed $m_1 \dots m_4$ inputs, the external field at which the output magnet can switch is

DOI:10.15774/PPKE.ITK.2018.003

$$B_z^{switch} = \pm B_z^{coer} + B_z^{cpl}. \tag{B.4}$$

Without coupling to inputs, the output magnet would switch at $\pm B_z^{coer}$ fields, i.e. at its intrinsic coercivity. The B_z^{cpl} coupling from the inputs alters the switching field: depending on the relative orientations of the output magnet's magnetization and the the sign of B_z^{cpl}, it may help or hinder the action of the external field.

So, if one applies an alternating field with B_z^{osc} amplitude along the z easy axis with a $B_z^{osc} \approx B_z^c$ amplitude, it will switch the output magnet into a direction determined by the sign of B_z^{cpl}:

$$m_{out} = \mathrm{sgn}(C_1 m_1 + C_2 m_2 + C_3 m_3 + C_4 m_3), \tag{B.5}$$

which is exactly the definition of threshold gate according to Eq. B.2 and the weights defined as $w_1 = C_1$, $w_2 = C_2$, etc.

If the magnetization states of all TLGs of an NML circuit satisfy Eq. B.5 (or a similar equation for a different type of TLG), then the B_z^{osc} external field can no longer switch the gate outputs. The coupling from the input arms stabilizes each gate outputs. In its computational ground state, the NML circuit is decoupled from the clocking field. If the NML circuit goes into a metastable state (for example, due to a new input), then the B_z^{osc} field drives out this metastable state after a few clocking cycles.

B.2 TLG based full adder

To show the efficiency and validate the proposed gate, we constructed and simulated a Full Adder (FA) based on two TGs. Fig. B.2 shows the schematic of the TG based FA. Note that the output values are inverted because of the antiferromagnetic coupling.

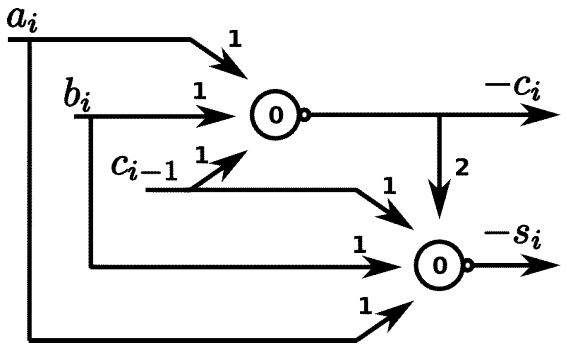

Figure B.2. Sketch of a TLG based Full Adder.

DOI:10.15774/PPKE.ITK.2018.003

We used $M_s = 6.8 \times 10^5$ A/m for the saturation magnetization of the Co/Pt magnets, $K_z = 3.42 \times 10^5$ J/m^3 for the uniaxial anisotropy constant, $A = 1.3 \times 10^{-11}$ J/m for exchange stiffness, and $\alpha = 0.05$ for the damping constant. These values are consistent with the volume averaged magnetic parameters of a Co/Pt films and similar to Co/Ni films. We assumed a d =10 nm film thickness.

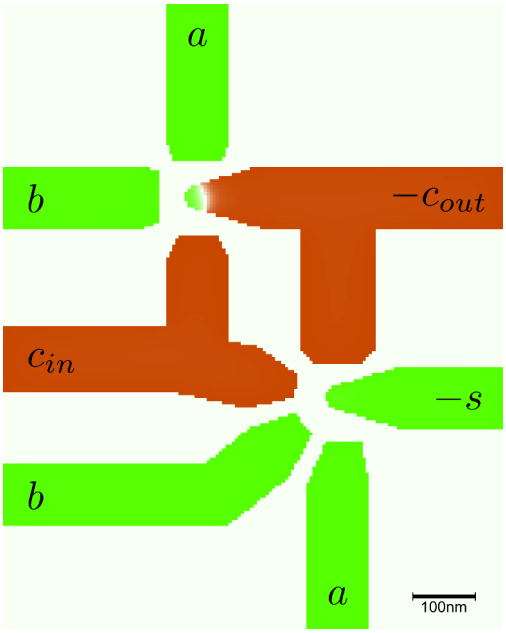

Figure B.3. The layout of the designed FA, the green color represents the −1 state $(A, B, -S)$, red is the +1 state $(C_{in}, -C_{out})$.

The nucleation center on the output arm is modeled as a low-anisotropy spot with a Gaussian distribution, with σ =15 nm, and with the lowest anisotropy at the center $K_z^{nucl} = K_z/2$. To speed up the DW propagation, a 80 mT constant external in-plane field was used. Using these parameters, we calculated a B_z^c =44 mT coercivity for the output magnet of Fig. B.1. Varying the K_z anisotropy parameter, a wide range of switching field values are achievable and the anisotropy of the irradiated spot can be considered as a design parameter.

The gate geometry of Fig. B.1 was designed to target $C_1 = -12$ mT and $C_2 = C_3 = C_4 = -6$ mT. The three-input gate was designed using the same procedure, and the target coupling fields for this gate (i.e. weights) were designed to be $C_1 = C_2 = C_3$ =8 mT. We used the magnetic field calculating engine of OOMMF to perform numerical magnetic field calculations, and simply adjusted the area of the input arms and their distance from the nucleation centers to until we reached the desired C_i values within 0.5 mT.

DOI:10.15774/PPKE.ITK.2018.003

Table B.1

SIMULATED SWITCHING FIELDS OF THE OUTPUTS

a	b	c_{in}	c_{out}	s	$B_z^{(c)}[mT]$	$B_z^{(s)}[mT]$
-1	-1	-1	1	1	18	39
-1	-1	1	1	-1	33	49
-1	1	-1	1	-1	34	49
-1	1	1	-1	1	49	38
1	-1	-1	1	-1	34	49
1	-1	1	-1	1	49	38
1	1	-1	-1	1	50	38
1	1	1	-1	-1	65	48

NOTE: The colors indicate whether the field of the inputs helps (green) or inhibits (red) the switching.

After designing the gate layout shown on Fig. B.3, we simulated the resulting TLG using all possible input combinations for the m_i input arm magnetizations in order to calculate the switching field of the output arm. The input fingers were kept fixed, while the B_z external field was swept in a quasi-static way. Table B.1 shows the such-calculated switching fields for both gates. For clocking field, we can choose any field that is higher than all green colored values, and smaller than all red values in Table B.1, i.e. the field has to be in the 39–48 mT range.

We simulated this layout for all possible input combinations, verifying that it indeed works for clocking fields $B^{osc} \approx 44$ mT. A few simulation snapshots are given in Fig. B.4. In this example, an up/down field cycle is sufficient to drive both threshold gates into the correct state. It can be shown that 2 field cycle is sufficient for all input combinations.

The simulation shows many details of the switching process that are out of the scope of the simple model we assumed. For example, it is visible in Fig. B.4 d) that the downwards pointing B_z^{osc} field affects the magnetic moments of the nucleation center of the three-input gate, but is unable to reverse its output. Considering the input/output relations however, the Full Adder works exactly as expected.

Based on our design, the device was experimentally realized at the Technische Universität München [1], and the AFM and MFM image of the structure can be seen in Fig. B.5. The layout is different from our design because it was optimized to the specific fabrication and measurement techniques. The functionality was tested and proved for all input combinations.

DOI:10.15774/PPKE.ITK.2018.003

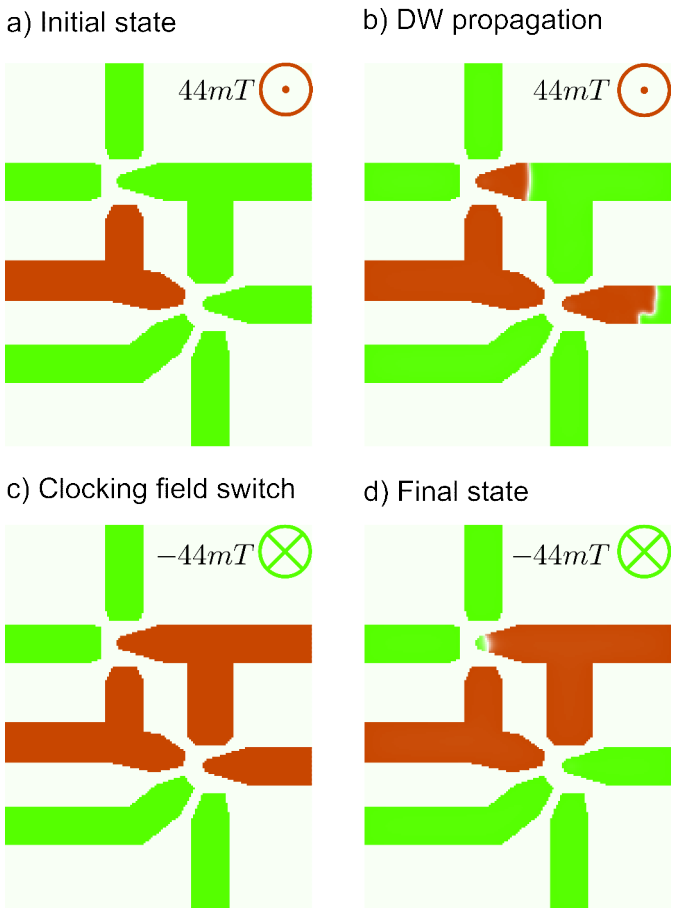

Figure B.4. Snapshots of a micromagnetic simulation of the threshold gate. The green color represents the -1 state $(A, B, -S)$, red is the $+1$ state $(C_{in}, -C_{out})$.

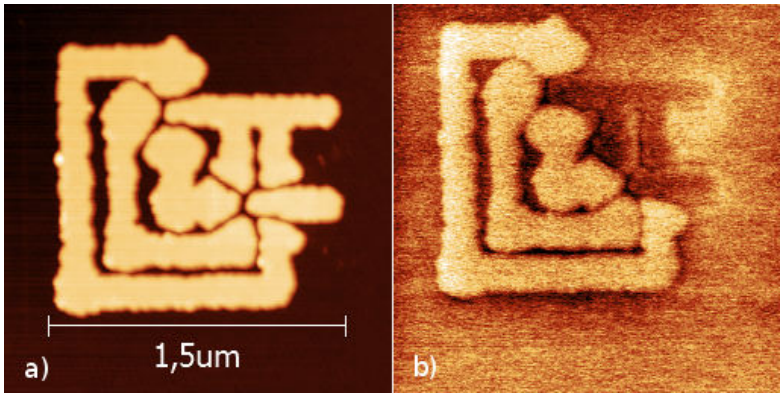

Figure B.5. AFM a) and MFM b) image of the physically implemented FA [1].

DOI:10.15774/PPKE.ITK.2018.003

B.3 Analysis

We estimate the robustness of the circuit based on the clocking window, i.e. the range of B^{osc} values that can properly switch the TLGs to their computational ground state. If the clocking window becomes narrow (i.e. comparable to the variations of the intrinsic dot switching field (B^{cpl}) of the dots) then it becomes impossible to find a B^{osc} field that drives all the magnets to their computational state.

Based on Table B.1, the clocking window $B^{window} \approx 11$ mT, and we assume that it could be optimized to get an even wider gap. The sources of variations are the variation of the coupling field B_z^{coer} which can be due to size and shape inaccuracy, and from other manufacturing variations, e.g. local changes in the multilayer compositions and the crystalline structure at the nucleation site. These can be improved by optimizing technology, but unlikely to go below few milliteslas [74]. In a larger circuit, it is generally not known what will be the state of farther-lying wire segments. The parasitic couplings (long-range stray fields) may "randomly" contribute the field acting in the nucleation center, and can significantly reduce the clocking window. Perhaps the most fundamental error source in NML is the thermally induced variation of B_z^{coer}, which also lies in the few-millitesla range [75].

We estimate that for the NML TLG simulated here, the clocking window is approximately two times bigger than the expected variations B_z^{coer}. This will result in error rates in the percentile range (10^{-2} error/switching) [74]. With stronger coupling fields and design procedures to reduce parasitic couplings, orders of magnitude improvements could be achievable.

In case of the full adder circuit, the TLG-based implementation can be realized on approximately half of the area (for comparison see [76]). Since power dissipation is proportional to the area of the circuit (where the B_z^{osc} field should be generated), this is also cut to half. Many (probably most) standard circuit designs would see a factor of 2-3 improvement in areal density and dissipation from the introduction of TLGs, so NML TLGs significantly improve the attractiveness of NML technology.

DOI:10.15774/PPKE.ITK.2018.003

PUBLICATIONS RESULTING FROM THIS DISSERTATION

1. G. Csaba, A. **Papp**, J. Chisum, W. Porod, and G. Bernstein, "Methods and apparatus for spin wave-based spectrum analyzers," U.S. Patent Application, 2017.

2. A. **Papp**, W. Porod, A. I. Csurgay, and G. Csaba, "Nanoscale spectrum analyzer based on spin-wave interference," *accepted to Scientific Reports*, 2017.

3. G. Csaba, A. **Papp**, and W. Porod, "Perspectives of using spin waves for computing and signal processing," *Physics Letters A*, Mar. 2017.

4. S. Breitkreutz-von Gamm, A. **Papp**, E. Egel, C. Meier, C. Yilmaz, L. Heis, W. Porod, and G. Csaba, "Design of On-Chip Readout Circuitry for Spin-Wave Devices," *IEEE Magnetics Letters*, vol. 8, pp. 1–4, 2017.

5. A. **Papp**, W. Porod, E. Song, and G. Csaba, "Wave-based signal processing devices using spin waves," in *CNNA 2016 15th International Workshop on Cellular Nanoscale Networks and their Applications*. Dresden, Germany: VDE Verlag GmbH, Aug. 2016.

6. A. **Papp**, G. Csaba, and W. Porod, "Optically-inspired computing based on spin waves," in *2016 IEEE International Conference on Rebooting Computing (ICRC)*. San Diego, CA, USA: IEEE, Oct. 2016, pp. 1–4.

7. ——, "Signal processing by spin-wave interference," in *Proceedings of International Conference on Microwave Magnetics*, Tuscaloosa, AL, USA, Jun. 2016.

8. E. Albisetti, D. Petti, M. Pancaldi, M. Madami, S. Tacchi, J. Curtis, W. P. King, A. **Papp**, G. Csaba, W. Porod, P. Vavassori, E. Riedo, and R. Bertacco, "Nanopatterning reconfigurable magnetic landscapes via thermally assisted scanning probe lithography," *Nature Nanotechnology*, Mar. 2016.

9. G. Csaba, A. **Papp**, W. Porod, and R. Yeniceri, "Non-boolean computing based on linear waves and oscillators," in *Solid State Device Research Conference (ESSDERC), 2015 45th European*. Graz, Austria: IEEE, 2015, pp. 101–104.

10. A. **Papp**, G. Csaba, and W. Porod, "Short-wavelength spin-wave generation by a microstrip line," in *Computational Electronics (IWCE), 2015 International Workshop on*. West Lafayette, IN, USA: IEEE, Sep. 2015, pp. 1–3.

11. A. **Papp**, W. Porod, and G. Csaba, "Hybrid yttrium iron garnet-ferromagnet structures for spin-wave devices," *Journal of Applied Physics*, vol. 117, no. 17, p. 17E101, May 2015.

12. A. **Papp**, M. T. Niemier, A. Csurgay, M. Becherer, S. Breitkreutz, J. Kiermaier, I. Eichwald, X. S. Hu, X. Ju, W. Porod, and G. Csaba, "Threshold Gate-Based Circuits From Nanomagnetic Logic," *IEEE Transactions on Nanotechnology*, vol. 13, no. 5, pp. 990–996, Sep. 2014.

13. A. **Papp**, G. Csaba, G. I. Bourianoff, and W. Porod, "Spin-Wave-Based Computing Devices," in *Nanotechnology (IEEE-NANO), 2014 IEEE 14th International Conference on*, Toronto, ON, Canada, Aug. 2014.

DOI:10.15774/PPKE.ITK.2018.003

14. G. Csaba, A. **Papp**, and W. Porod, "Signal processing with optically-inspired algorithms," in *CNNA 2014 14th International Workshop on Cellular Nanoscale Networks and their Applications*. Notre Dame, IN, USA: IEEE, Jul. 2014, pp. 1–2.

15. S. Breitkreutz, I. Eichwald, J. Kiermaier, A. **Papp**, G. Csaba, M. Niemier, W. Porod, D. Schmitt-Landsiedel, and M. Becherer, "1-Bit Full Adder in Perpendicular Nanomagnetic Logic using a Novel 5-Input Majority Gate," *EPJ Web of Conferences*, vol. 75, p. 05001, 2014.

16. G. Csaba, A. **Papp**, and W. Porod, "Spin-wave based realization of optical computing primitives," *Journal of Applied Physics*, vol. 115, no. 17, p. 17C741, May 2014.

17. ——, "Holographic algorithms for on-chip, non-boolean computing," in *Computational Electronics (IWCE), 2014 International Workshop on*. Paris: IEEE, Jun. 2014, pp. 1–2.

18. A. **Papp**, G. Csaba, and W. Porod, "Non-Boolean Computing Using Spin Waves," in *Abstracts of IWCE*, Nara, Japan, Jun. 2013, pp. 78–79.

19. G. Csaba, A. **Papp**, A. Csurgay, and W. Porod, "Simulation of domain-wall assisted magnetic ordering," in *Abstracts of IWCE*, Madison, USA, May 2012, pp. 261–262.

DOI:10.15774/PPKE.ITK.2018.003

Bibliography

1. S. Breitkreutz, J. Kiermaier, I. Eichwald, C. Hildbrand, G. Csaba, D. Schmitt-Landsiedel, and M. Becherer, "Experimental Demonstration of a 1-Bit Full Adder in Perpendicular Nanomagnetic Logic," *IEEE Transactions on Magnetics*, vol. 49, no. 7, pp. 4464–4467, Jul. 2013.

2. A. Imre, G. Csaba, L. Ji, A. Orlov, G. H. Bernstein, and W. Porod, "Majority Logic Gate for Magnetic Quantum-Dot Cellular Automata," *Science*, vol. 311, no. 5758, pp. 205–208, Jan. 2006.

3. I. Eichwald, S. Breitkreutz, G. Ziemys, G. Csaba, W. Porod, and M. Becherer, "Majority logic gate for 3d magnetic computing," *Nanotechnology*, vol. 25, no. 33, p. 335202, Aug. 2014.

4. A. Khitun and K. L. Wang, "Nano scale computational architectures with Spin Wave Bus," *Superlattices and Microstructures*, vol. 38, no. 3, pp. 184–200, Sep. 2005.

5. G. Csaba, M. Pufall, D. E. Nikonov, G. I. Bourianoff, A. Horvath, T. Roska, and W. Porod, "Spin torque oscillator models for applications in associative memories." IEEE, Aug. 2012, pp. 1–2.

6. G. Csaba and W. Porod, "Computational Study of Spin-Torque Oscillator Interactions for Non-Boolean Computing Applications," *IEEE Transactions on Magnetics*, vol. 49, no. 7, pp. 4447–4451, Jul. 2013.

7. A. V. Chumak, A. A. Serga, and B. Hillebrands, "Magnon transistor for all-magnon data processing," *Nature Communications*, vol. 5, p. 4700, Aug. 2014.

8. T. Schneider *et al.*, "Realization of spin-wave logic gates," *Applied Physics Letters*, vol. 92, 2008.

9. A. V. Chumak, V. Vasyuchka, A. Serga, and B. Hillebrands, "Magnon spintronics," *Nature Physics*, vol. 11, no. 6, pp. 453–461, Jun. 2015.

10. G. Csaba, A. Papp, and W. Porod, "Perspectives of using spin waves for computing and signal processing," *Physics Letters A*, Mar. 2017.

11. R. Yeniceri and M. Yalcin, "An emulated digital wave computer core implementation." IEEE, Aug. 2009, pp. 831–834.

12. A. Kriman and G. Bernstein, "Quadfet-a novel field effect transistor," Patent, Oct., 1990, uS Patent 4,962,410. [Online]. Available: https://www.google.com/patents/US4962410

13. W. Ishak, "Magnetostatic wave technology: a review," *Proceedings of the IEEE*, vol. 76, no. 2, pp. 171–187, Feb. 1988.

14. J. A. Stankovic, "Research Directions for the Internet of Things," *IEEE Internet of Things Journal*, vol. 1, no. 1, pp. 3–9, Feb. 2014.

15. M. J. Donahue and D. G. Porter, *OOMMF User's Guide, Version 1.2a3*. National Institute of Standards and Technology, Gaithersburg, MD, 1999, interagency Report NISTIR 6376. [Online]. Available: http://math.nist.gov/oommf/

16. A. Vansteenkiste, J. Leliaert, M. Dvornik, M. Helsen, F. Garcia-Sanchez, and B. Van Waeyenberge, "The design and verification of MuMax3," *AIP Advances*, vol. 4, no. 10, p. 107133, Oct. 2014.

17. H. Yu, O. d. Kelly, V. Cros, R. Bernard, P. Bortolotti, A. Anane, F. Brandl, R. Huber, I. Stasinopoulos, and D. Grundler, "Magnetic thin-film insulator with ultra-low spin wave damping for coherent nanomagnonics," *Scientific Reports*, vol. 4, p. 6848, Oct. 2014.

18. D. D. Stancil and A. Prabhakar, *Spin Waves: Theory and Applications*. Springer London, Limited, 2009.

19. J. W. Kłos and M. Krawczyk, "Magnonic Crystals: From Simple Models toward Applications," *Magnetic Structures of 2D and 3D Nanoparticles: Properties and Applications*, p. 283, 2016.

20. M. Madami, S. Bonetti, G. Consolo, S. Tacchi, G. Carlotti, G. Gubbiotti, F. B. Mancoff, M. A. Yar, and J. Akerman, "Direct observation of a propagating spin wave induced by spin-transfer torque," *Nature Nanotechnology*, vol. 6, no. 10, pp. 635–638, Aug. 2011.

21. S. E. Russek *et al.*, "Spin-transfer nano-oscillators," in *Handbook of nanophysics: Functional Nanomaterials*, K. D. Sattler, Ed. Addison Wesley, 2010, p. 10.

22. B. Lenk, H. Ulrichs, F. Garbs, and M. Münzenberg, "The building blocks of magnonics," *Physics Reports*, vol. 507, no. 4-5, pp. 107–136, Oct. 2011.

23. V. V. Kruglyak, S. O. Demokritov, and D. Grundler, "Magnonics," *Journal of Physics D: Applied Physics*, vol. 43, no. 26, p. 264001, Jul. 2010.

24. M. J. Riedl, *Optical design fundamentals for infrared systems*, 2nd ed., ser. Tutorial texts in optical engineering. Bellingham, Wash: SPIE Press, 2001, no. TT 48.

25. D. Jeon, M. Seok, C. Chakrabarti, D. Blaauw, and D. Sylvester, "A super-pipelined energy efficient subthreshold 240 MS/s FFT core in 65 nm CMOS," *IEEE Journal of Solid-State Circuits*, vol. 47, no. 1, pp. 23–34, Jan. 2012.

26. A. Papp, W. Porod, a. I. Csurgay, and G. Csaba, "Nanoscale spectrum analyzer based on spin-wave interference," *accepted to Scientific Reports*, 2017.

27. T. Schneider, A. A. Serga, B. Leven, B. Hillebrands, R. L. Stamps, and M. P. Kostylev, "Realization of spin-wave logic gates," *Applied Physics Letters*, vol. 92, no. 2, p. 022505, 2008.

28. A. Khitun, "Magnonic holographic devices for special type data processing," *Journal of Applied Physics*, vol. 113, no. 16, p. 164503, 2013.

29. F. Gertz, A. Kozhevnikov, Y. Filimonov, and A. Khitun, "Magnonic Holographic Memory," *IEEE Transactions on Magnetics*, pp. 1–1, 2014.

30. H. Chang, L. P., W. Zhang, T. Liu, A. Hoffmann, L. Deng, and M. Wu, "Nanometer-thick yttrium iron garnet films with extremely low damping." *IEEE Magnetics Letters.*, vol. 5, no. 1-4, 2014.

31. E. Afshari, H. Bhat, and A. Hajimiri, "Ultrafast Analog Fourier Transform Using 2-D LC Lattice," *IEEE Transactions on Circuits and Systems I: Regular Papers*, vol. 55, no. 8, pp. 2332–2343, Sep. 2008.

32. J. Uher and W. Hoefer, "Tunable microwave and millimeter-wave band-pass filters," *IEEE Transactions on Microwave Theory and Techniques*, vol. 39, no. 4, pp. 643–653, Apr. 1991.

33. S. Hanna, "Apparatus and method for diffracting MSW in a garnet film using SAW," Patent, Oct., 1991. [Online]. Available: https://www.google.com/patents/US5057800

34. M. C. Hutley, *Diffraction gratings*, ser. Techniques of physics. London: Academic Press, 1982, no. 6.

35. J. James, *James J. Spectrograph design fundamentals*. Cambridge University Press, 2007.

36. A. G. Gurevich and G. A. Melkov, *Magnetization oscillations and waves*. CRC press, 1996.

37. J. Schwartz, I. Arnedo, M. A. G. Laso, T. Lopetegi, J. Azana, and D. Plant, "An electronic uwb continuously tunable time-delay system with nanosecond delays," *IEEE Microwave and Wireless Components Letters*, vol. 18, no. 2, pp. 103–105, 2008.

38. M. Covington, T. M. Crawford, and G. J. Parker, "Time-Resolved Measurement of Propagating Spin Waves in Ferromagnetic Thin Films," *Physical Review Letters*, vol. 89, no. 23, Nov. 2002.

39. J. W. Goodman, *Introduction to Fourier optics*, 2nd ed., ser. McGraw-Hill series in electrical and computer engineering. New York: McGraw-Hill, 1996.

40. C. Hahn, V. V. Naletov, G. de Loubens, O. Klein, O. d'Allivy Kelly, A. Anane, R. Bernard, E. Jacquet, P. Bortolotti, V. Cros, J. L. Prieto, and M. Muñoz, "Measurement of the intrinsic damping constant in individual nanodisks of Y3fe5o12 and Y3fe5o12|Pt," *Applied Physics Letters*, vol. 104, no. 15, p. 152410, Apr. 2014.

41. H. Yu, G. Duerr, R. Huber, M. Bahr, T. Schwarze, F. Brandl, and D. Grundler, "Omnidirectional spin-wave nanograting coupler," *Nature Communications*, vol. 4, Nov. 2013.

42. S. Breitkreutz, A. Papp, E. Egel, C. Meier, C. Yilmaz, L. Heiss, W. Porod, and G. Csaba, "Design of on-chip readout circuitry for spin-wave devices," *IEEE Magnetics Letters*, pp. 1–1, 2016.

43. J. D. Adam and S. N. Stitzer, "A magnetostatic wave signal-to-noise enhancer," *Applied Physics Letters*, vol. 36, no. 6, p. 485, 1980.

44. S. Cherepov *et al.*, "Electric-field-induced spin wave generation using multiferroic magnetoelectric cells," *Applied Physics Letters*, vol. 104, no. 8, Feb. 2014.

45. P. Li, H. Chang, K. A., W. Zhang, G. Csaba, W. Li, D. Richardson, D. A., R. G., H. Dey, J. JS, P. W., S. Field, T. J. abd Marconi M., H. A., and M. Mryasov O.and Wu, "Spin-orbit torque-assisted switching in magnetic insulator thin films with perpendicular magnetic anisotropy," *Nature communications*, vol. 7, no. 1-4, 2016.

46. M. Balinsky, H. M., R. M., P. Durrenfeld, H. A., and S. A. A. J., "Modulation of the spectral characteristics of a nano- contact spin-torque oscillator via spin waves in an adjacent yttrium-iron garnet film," *IEEE Magnetics Letters*, vol. 7, no. 7, Apr. 2016.

47. G. Csaba, A. Papp, and W. Porod, "Spin-wave based realization of optical computing primitives," *Journal of Applied Physics*, vol. 115, no. 17, p. 17C741, May 2014.

48. A. V. Chumak, A. A. Serga, M. B. Jungfleisch, R. Neb, D. A. Bozhko, V. S. Tiberkevich, and B. Hillebrands, "Direct detection of magnon spin transport by the inverse spin Hall effect," *Applied Physics Letters*, vol. 100, no. 8, p. 082405, 2012.

DOI:10.15774/PPKE.ITK.2018.003

49. J. Russer, N. Uddin, A. Awny, A. Thiede, and P. Russer, "Near-field measurement of stochastic electromagnetic fields," *IEEE Electronic Compatibility Magazine*, vol. 4, no. 5, Apr. 2015.

50. A. V. Chumak, V. Vasyuchka, A. Serga, and B. Hillebrands, "Magnon spintronics," *Nature Physics*, vol. 11, no. 6, pp. 453–461, Jun. 2015.

51. A. Papp, W. Porod, and G. Csaba, "Hybrid yttrium iron garnet-ferromagnet structures for spin-wave devices," *Journal of Applied Physics*, vol. 117, no. 17, p. 17E101, May 2015.

52. A. Khitun, D. E. Nikonov, M. Bao, K. Galatsis, and K. L. Wang, "Efficiency of Spin-Wave Bus for Information Transmission," *IEEE Transactions on Electron Devices*, vol. 54, no. 12, pp. 3418–3421, 2007.

53. A. A. Serga, A. V. Chumak, and B. Hillebrands, "YIG magnonics," *Journal of Physics D: Applied Physics*, vol. 43, no. 26, p. 264002, Jul. 2010.

54. R. Suzuki, M. Takahashi, T. Kobayashi, and Y. Sugita, "Planar domains and domain wall structures of bubbles in Permalloy-coated garnet films," *Applied Physics Letters*, vol. 26, no. 6, p. 342, 1975.

55. J. Ben Youssef, V. Castel, N. Vukadinovic, and M. Labrune, "Spin-wave resonances in exchange-coupled Permalloy/garnet bilayers," *Journal of Applied Physics*, vol. 108, no. 6, p. 063909, 2010.

56. N. Vukadinovic, J. Ben Youssef, V. Castel, and M. Labrune, "Magnetization dynamics in interlayer exchange-coupled in-plane/out-of-plane anisotropy bilayers," *Physical Review B*, vol. 79, no. 18, May 2009.

57. O. d'Allivy Kelly, A. Anane, R. Bernard, J. Ben Youssef, C. Hahn, A. H. Molpeceres, C. Carrétéro, E. Jacquet, C. Deranlot, P. Bortolotti, R. Lebourgeois, J.-C. Mage, G. de Loubens, O. Klein, V. Cros, and A. Fert, "Inverse spin Hall effect in nanometer-thick yttrium iron garnet/Pt system," *Applied Physics Letters*, vol. 103, no. 8, p. 082408, 2013.

58. Y. S. Chun, "Interlayer perpendicular domain coupling between thin Fe films and garnet single-crystal underlayers," *Journal of Applied Physics*, vol. 95, no. 11, p. 6858, 2004.

59. J. F. Cochran, B. Heinrich, and A. S. Arrott, "Ferromagnetic resonance in a system composed of a ferromagnetic substrate and an exchange-coupled thin ferromagnetic overlayer," *Physical Review B*, vol. 34, no. 11, pp. 7788–7801, Dec. 1986.

60. S. Klingler, A. V. Chumak, T. Mewes, B. Khodadadi, C. Mewes, C. Dubs, O. Surzhenko, B. Hillebrands, and A. Conca, "Measurements of the exchange stiffness of YIG films using broadband ferromagnetic resonance techniques," *Journal of Physics D: Applied Physics*, vol. 48, no. 1, p. 015001, Jan. 2015.

61. A. G. Temiryazev, M. P. Tikhomirova, and P. E. Zil'berman, ""Exchange" spin waves in nonuniform yttrium iron garnet films," *Journal of Applied Physics*, vol. 76, no. 9, p. 5586, 1994.

62. G. Gubbiotti, S. Tacchi, M. Madami, G. Carlotti, A. O. Adeyeye, and M. Kostylev, "Brillouin light scattering studies of planar metallic magnonic crystals," *Journal of Physics D: Applied Physics*, vol. 43, no. 26, p. 264003, Jul. 2010.

63. M. Balinsky, M. Haidar, M. Ranjbar, P. Durrenfeld, A. Houshang, A. Slavin, and J. Akerman, "Modulation of the Spectral Characteristics of a Nano-Contact Spin-Torque Oscillator via Spin Waves in an Adjacent Yttrium-Iron Garnet Film," *IEEE Magnetics Letters*, vol. 7, pp. 1–4, 2016.

DOI:10.15774/PPKE.ITK.2018.003

64. A. B. Kos, T. J. Silva, and P. Kabos, "Pulsed inductive microwave magnetometer," *Review of Scientific Instruments*, vol. 73, no. 10, pp. 3563–3569, Oct. 2002.

65. T. Liu, H. Chang, V. Vlaminck, Y. Sun, M. Kabatek, A. Hoffmann, L. Deng, and M. Wu, "Ferromagnetic resonance of sputtered yttrium iron garnet nanometer films," *Journal of Applied Physics*, vol. 115, no. 17, p. 17A501, May 2014.

66. G. Gubbiotti, G. Carlotti, M. Madami, S. Tacchi, P. Vavassori, and G. Socino, "Setup of a new Brillouin light scattering apparatus with submicrometric lateral resolution and its application to the study of spin modes in nanomagnets," *Journal of Applied Physics*, vol. 105, no. 7, p. 07D521, Apr. 2009.

67. A. A. Serga, T. Schneider, B. Hillebrands, S. O. Demokritov, and M. P. Kostylev, "Phase-sensitive Brillouin light scattering spectroscopy from spin-wave packets," *Applied Physics Letters*, vol. 89, no. 6, p. 063506, Aug. 2006.

68. A. Papp, M. T. Niemier, A. I. Csurgay, M. Becherer, S. Breitkreutz, J. Kiermaier, I. Eichwald, X. S. Hu, X. Ju, W. Porod, and G. Csaba, "Threshold gate based circuits from nanomagnetic logic," *submitted to IEEE Transactions on Nanotechnology*, 2013.

69. E. Varga, G. Csaba, G. Bernstein, and W. Porod, "Implementation of a nanomagnetic full adder circuit," in *Nanotechnology (IEEE-NANO), 2011 11th IEEE Conference on*. IEEE, 2011, pp. 1244–1247.

70. D. Hampel and R. O. Winder, "Threshold logic," *IEEE Spectrum*, vol. 8, no. 5, pp. 32–39, May 1971.

71. Q. Sheng, *Threshold logic*. Toronto; The Ryerson; New York; London: Academic Press, 1969.

72. J. H. Cyprus, "Optimal synthesis of the boolean functions of four variables with majority logic," PhD dissertation, Rice University, Texas, 1964. [Online]. Available: http://hdl.handle.net/1911/62874

73. C. Lageweg, S. Cotofana, and S. Vassiliadis, "A full adder implementation using SET based linear threshold gates," in *Electronics, Circuits and Systems, 2002. 9th International Conference on*, vol. 2. IEEE, 2002, pp. 665–668.

74. S. Breitkreutz, J. Kiermaier, C. Yilmaz, X. Ju, G. Csaba, D. Schmitt-Landsiedel, and M. Becherer, "Nanomagnetic logic: compact modeling of field-coupled computing devices for system investigations," *Journal of Computational Electronics*, vol. 10, no. 4, pp. 352–359, 2011.

75. G. Csaba and W. Porod, "Behavior of nanomagnet logic in the presence of thermal noise," in *Computational Electronics (IWCE), 2010 14th International Workshop on*. IEEE, 2010, pp. 1–4.

76. S. Breitkreutz, J. Kiermaier, I. Eichwald, C. Hildbrand, G. Csaba, D. Schmitt-Landsiedel, and M. Becherer, "Experimental demonstration of a 1-bit full adder in perpendicular nanomagnetic logic," in *accepted for Intermag / MMM*, Chicago, IL, 2013.

The project was supported by the European Union, co-financed by the European Social Fund (EFOP-3.6.3-VEKOP-16-2017-00002).